NANOSTRUCTURAL ANALYSIS OF CUBIC GaN AND CUBIC InN FILMS BY TRANSMISSION ELECTRON MICROSCOPY

Miss Jamreonta Parinyataramas

A Dissertation Submitted in Partial Fulfillment of the Requirements
for the Degree of Doctor of Philosophy Program in Nanoscience and Technology
(Interdisciplinary Program)
Graduate School
Chulalongkorn University
Academic Year 2011

การวิเคราะห์โครงสร้างระดับนาโนของฟิล์มคิวบิกแกลเลียมไนไตรด์และคิวบิกอินเดียมไนไตรด์โดยกล้องจุลทรรศน์อิเล็กตรอนชนิดส่องผ่าน

นางสาวจำเริญตา ปริญญาธารมาศ

วิทยานิพนธ์นี้เป็นส่วนหนึ่งของการศึกษาตามหลักสูตรปริญญาวิทยาศาสตรดุษฎีบัณฑิต
สาขาวิชาวิทยาศาสตร์นาโนและเทคโนโลยี (สหสาขาวิชา)
บัณฑิตวิทยาลัย จุฬาลงกรณ์มหาวิทยาลัย
ปีการศึกษา 2554

Thesis Title	NANOSTRUCTURAL ANALYSIS OF CUBIC GaN AND CUBIC InN FILMS BY TRANSMISSION ELECTRON MICROSCOPY
By	Miss Jamreonta Parinyataramas
Field of Study	Nanoscience and Technology
Thesis Advisor	Assistant Professor Sakuntam Sanorpim, Ph.D.
Thesis Co-advisor	Chanchana Thanachayanont, Ph.D.

Accepted by the Graduate School, Chulalongkorn University in Partial Fulfillment of the Requirements for the Doctoral Degree

…….. Dean of the Graduate School

(Associate Professor Pornpote Piumsomboon, Ph.D.)

THESIS COMMITTEE

…….. Chairman

(Associate Professor Vudhichai Parasuk, Ph.D.)

…….. Thesis Advisor

(Assistant Professor Sakuntam Sanorpim, Ph.D.)

…….. Thesis Co-advisor

(Chanchana Thanachayanont, Ph.D.)

…….. Examiner

(Associate Professor Pornthep Sompornpisut, Ph.D.)

…….. Examiner

(Stephan Thierry Dubas, Ph.D.)

…….. External Examiner

(Noppadon Nuntawong, Ph.D.)

จำเริญตา ปริญญาธารมาศ : การวิเคราะห์โครงสร้างระดับนาโนของฟิล์มคิวบิกแกลเลียมไนไตรด์และคิวบิกอินเดียมไนไตรด์โดยกล้องจุลทรรศน์อิเล็กตรอนชนิดส่องผ่าน (NANOSTRUCTURAL ANALYSIS OF CUBIC GaN AND CUBIC InN FILMS BY TRANSMISSION ELECTRON MICROSCOPY
อ. ที่ปรึกษาวิทยานิพนธ์หลัก : ผศ. ดร.สกุลธรรม เสนาะพิมพ์, อ. ที่ปรึกษาวิทยานิพนธ์ร่วม : ดร. ชัญชณา ธนชยานนท์, 93 หน้า.

ได้ดำเนินการวิเคราะห์เชิงโครงสร้างในระดับนาโนสเกลของฟิล์มบางคิวบิกเฟสแกลเลียมไนไตรด์ (c-GaN) และ อินเดียมไนไตรด์ (c-InN) โดยกล้องจุลทรรศน์อิเล็กตรอนชนิดส่องผ่าน (TEM) เพื่อตรวจสอบการเปลี่ยนโครงสร้างเฟส และการเกิดความบกพร่องเชิงโครงสร้าง ซึ่งอาจเป็นผลกระทบจากความคล้ายของโครงสร้างระหว่างคิวบิกระนาบ (111) และเฮกซะโกนัลระนาบ (0001) โดยการหมุน 60 องศา การศึกษานี้พบว่าการแทรกชั้นบัฟเฟอร์ เป็นวิธีที่ใช้แล้วประสบความสำเร็จในการปกป้องซับสเตรต GaAs ที่มีผิวระนาบ (001) จากการแตกสลายด้วยความร้อนซึ่งก่อเกิดขั้น (step) ระนาบ (111) บนผิวหน้า GaAs ระนาบ (001) ส่งผลในการเปลี่ยนโครงสร้างเฟสจากคิวบิกเป็นเฟสผสมคิวบิก/เฮกซะโกนัลในฟิล์มคิวบิกไนไตรด์ นอกจากนี้ความไม่สม่ำเสมอของขั้นระนาบ (111) ตามแนวทิศทาง [110] และ [1$\bar{1}$0] ของชั้นบัฟเฟอร์ก่อเกิดการกระจายตัวในความไม่สม่ำเสมอของความบกพร่องที่สังเกตได้จากภาพชนิดภาคตัดขวางที่วัดจาก TEM ตามแนวแกน [110] และ [1$\bar{1}$0] ชนิดของความบกพร่องขึ้นกับแนวแกนเนื่องจากความไม่สม่ำเสมอโครงสร้างอะตอมที่เป็นขั้นในระนาบ (001) ของผิวหน้าชั้นบัฟเฟอร์อะลูมิเนียมแกลเลียมอาร์เซไนด์ (AlGaAs) ภาพชนิดภาคตัดขวางที่วัดจาก TEM ตามแนวแกน [1$\bar{1}$0] แสดงสแตกกิงฟอลท์ (stacking faults) จำนวนน้อยแต่พบทวิน (twin) ของคิวบิกโดยการวางตัวของอิพิแทกซีในทิศทาง $[\bar{1}1\bar{4}]_{\text{ทวินของคิวบิก}}//[110]_{\text{ซับสเตรต}}$ มีเฉพาะดิสโลเคชันแนวตรงถูกพบที่บริเวณส่วนบนของชั้นฟิล์ม การมีทวินของคิวบิกก่อให้เกิดบริเวณแอนติเฟสโดเมนในชั้นฟิล์ม สำหรับฟิล์มบาง c-InN บนซับสเตรตแมกนีเซียมออกไซด์ (MgO) ที่มีผิวระนาบ (001) ที่มีบัฟเฟอร์ c-GaN เงื่อนไขการปลูกที่มีอินเดียมในปริมาณมากเกินพอช่วยพัฒนาคุณภาพผลึกของการปลูกชั้น c-InN การเกิดเฟสเฮกซะโกนัลลดลงโดยเพิ่มอุณหภูมิการปลูกและฟลักซ์ของอินเดียม อย่างไรก็ตามการเปลี่ยนโครงสร้างเฟสจากคิวบิกเป็นเฟสผสมคิวบิก/เฮกซะโกนัลใน c-InN ให้ฟิล์มที่คุณภาพดีที่สุด แสดงในรูปของความบกพร่องเชิงระนาบเช่นสแตกกิงฟอลท์และทวินซึ่งก่อเกิดจากรอยต่อระหว่างชั้นบัฟเฟอร์ c-GaN และชั้นฟิล์ม c-InN

สาขาวิชา วิทยาศาสตร์นาโนและเทคโนโลยี ลายมือชื่อนิสิต .....
ปีการศึกษา 2554 ลายมือชื่อ อ.ที่ปรึกษาวิทยานิพนธ์หลัก.....
ลายมือชื่อ อ.ที่ปรึกษาวิทยานิพนธ์ร่วม .....

#4989726720: MAJOR NANOSCIENCE AND TECHNOLOGY
KEYWORDS: CUBIC GaN/ CUBIC InN/ CUBIC STRUCTURE/ TEM/ HEXAGONAL PHASE

JAMREONTA PARINYATARAMAS: NANOSTRUCTURAL ANALYSIS OF CUBIC GaN AND CUBIC InN FILMS BY TRANSMISSION ELECTRON MICROSCOPY. ADVISOR: ASST. PROF. SAKUNTAM SANORPIM, Ph.D., CO-ADVISOR: CHANCHANA THANACHAYANONT, Ph.D., 93 pp.

Structural analysis of the cubic-phase GaN (c-GaN) and InN (c-InN) thin films was performed in nano-scale using transmission electron microscopy (TEM) to verify the structural-phase transformation and the structural defect formation, which may be affected by the structural similarities between the cubic (111) and hexagonal (0001) planes with rotating 60°. This study found out that the insertion of buffer layer is a successful method to protect the (001) GaAs substrate from thermal decomposition, which introduces the (111) stepped on (001) GaAs surface. This results in a structural-phase transformation from cubic to mixed cubic/hexagonal-phases in the cubic nitride films. Moreover, an anisotropic (111) steps along the [110] and [1$\bar{1}$0] direction of the buffer layer induced anisotropic distribution of defects observed in cross-sectional TEM images taken along the [110] and [1$\bar{1}$0] zone axes. Zone axis dependent type of defects is due to a different atomic structure of surface step on the (001) AlGaAs buffer layer. Cross-sectional TEM images taken along [1$\bar{1}$0] zone axis show a less stacking faults (SFs) but appear a cubic twin with an epitaxial orientation of $[\bar{1}1\bar{4}]_{\text{cubic twin}}//[110]_{\text{substrate}}$. Only some treading dislocations were observed on top region of the layer. A present of cubic twin also induced an anti-phase domain boundary in the layer. For the c-InN thin films on MgO (001) substrate with a c-GaN buffer, the In-rich growth condition was found to improve the crystal quality of the c-InN grown layer. Hexagonal phase generation decreased with increasing growth temperature and In flux. However, the structural-phase transformation from cubic to mixed cubic/hexagonal phases in the best quality c-InN films exhibited in a form of planar defects, such as stacking faults and twins generated from the interface between the c-GaN buffer layer and the c-InN film.

Field of Study :Nanoscience and Technology Student's Signature .....

Academic Year : .....2011..... Advisor's Signature .....

Co-advisor's Signature .....

ACKNOWLEDGEMENTS

I would like to fully appreciate my advisor, Assistance Professor Dr. Sakuntam Sanorpim and Dr. Chanchana Thanachayanont for their valuable suggestion and their support in everything about this thesis. They always give me a good attention and valuable experience during my study.

I would like to acknowledge my thesis committee Associate Professor Dr. Vudhichai Parasuk, Associate Professor Dr. Pornthep Sompornpisut, Dr. Stephan Thierry Dubas and Dr. Noppadon Nuntawong for their time and their comment on this thesis.

I would like to thank National Metal and Materials Technology Center (MTEC) for facilities in using instrument and Mr. Visittapong Yordsri for a suggestion to prepare sample for TEM analysis and his technical assistance in TEM operation.

Special thank goes to Nanoscience and Technology program, Graduate School, Chulalongkorn University for their financial support to international conference.

I would like to thank my friends and my junior friends for helpful discussion and joyful moments.

Lastly, I would like to appreciate my family: my father, my mother and my sister for their love, support and understanding.

Contents

List of Tables

List of Figures

Figure **Page**

Figure **Page**

Figure **Page**

Figure **Page**

CHAPTER I

INTRODUCTION

1.1 Overview of GaN and InN

The present strong interest in group III-Nitride semiconductors, such as GaN, InN and their alloy InGaN, was triggered by key discoveries several ten years ago [1, 2]. The use of low temperature buffer layers in epitaxial growth of GaN turned out to be a major step towards rearing device grade material quality [3]. Moreover, recent developments of the growth technique, such as metalorganic vapor phase epitaxy (MOVPE) and molecular beam epitaxy (MBE), provide InN thin films with higher quality [4]. This leads to a large variation of bandgap in the range between 0.6 to 3.3 eV by alloying InN with GaN [5]. These unique properties have made these materials to be promising materials for optoelectronic device applications in the infrared to ultra-violet wavelength ranges, such as light emitting diodes (LEDs) and laser diodes (LDs) in green, blue, ultraviolet and white light emitters [6-9]. The relation between bandgap of the III-nitride semiconductors, their wavelength and lattice constant are summarized in Fig.1.1. Moreover, they have attracted as candidates for high power and high frequency applications such as cellular phones and satellite communications (0.8-1.9 GHz) [11]. The binary InN and InGaN alloys have potential applications as light emitter for fiber optic communication and solar cells [12]. In particular, the ideal candidates for optical fibers are In-rich $In_xGa_{1-x}N$ due to the fact that the indium

composition can be controlled leading to longer wavelengths in the range between 1.3 to 1.5 μm [13]. There have been reports that both GaN and InN preferably crystalize in two structural phases, i.e. wurtzite (hexagonal) and zincblend (cubic) structures [14]. Hexagonal-phase GaN (h-GaN) has been successfully applied in fabrication of high-brightness LEDs due to its stable structure, which leads to commercially availability [15].

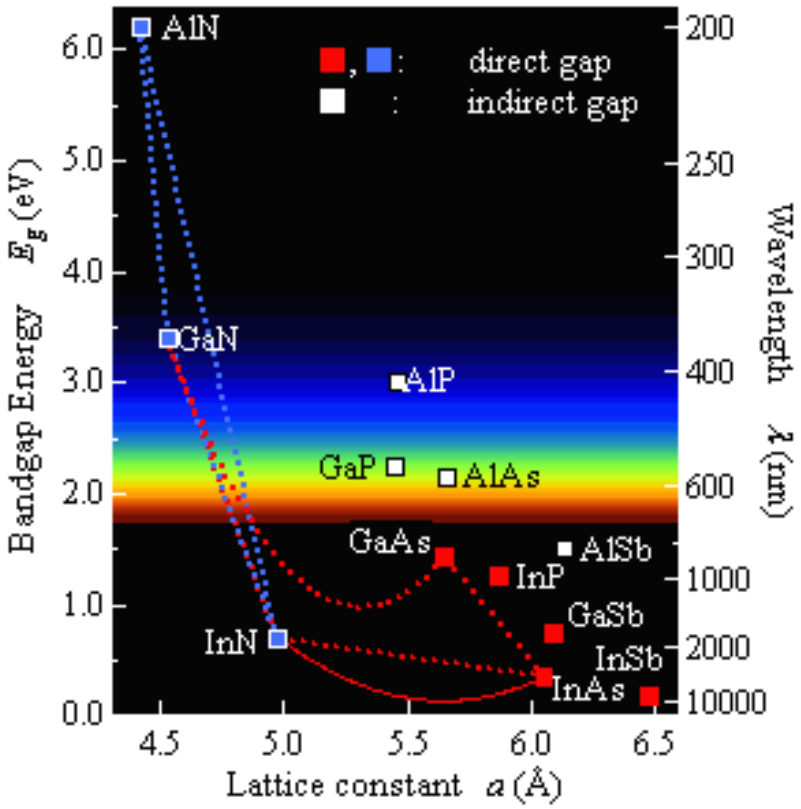

Figure 1.1: Relation between Bandgap, Lattice constant and Wavelength of group III-Nitride semiconductors [10] compared to conventional III-V semiconductors, i.e. InAs, GaAs.

The imbalance of research on these two structural phases for both GaN and InN is resulted from the difficulty of the growth of high quality metastable cubic-phase GaN

(c-GaN) and InN (c-InN) [16]. Despite the fact that metastable c-GaN crystal is expected to have superior electronic properties, such as lower resistivity and lower electron effective mass, because of its higher crystallographic symmetry resulting in a reduction of electron-phonon scattering [17-20]. Further, it is also expected to have higher doping efficiency [17]. The c-InN crystal is also expected to have such superior electronic properties as for the c-GaN crystal. Interest in InN is increasing due to their excellent optical and electrical properties such as high-speed electronic devices and full-color display [21]. Outstanding property of InN is the smallest effective mass with the highest saturation electron velocity that makes them suitable for electronic applications such as high performance hetero-junction field effect transistors and high-efficiency solar-cells [22]. The InN was first synthesised in 1938 by Juza and Hahn [23]. There are many researches that have been developed for the growth technology of InN to obtain InN crystal with high crystalline quality. Recently, the energy gap of InN was accepted ~ 0.7 eV [24, 25]. However, the high quality of these metastable c-GaN and c-InN is known to be difficult to prepare. The first reason is that the cubic phase nitrides are less stable compared with hexagonal phase nitrides. This is based on the fact that, there are similarity between c-GaN in direction <111> and h-GaN in direction <0001> by rotating 60°, which leads to a structural phase transition from cubic to hexagonal structure along the <111> direction. Moreover, due to the lack of an appropriate substrate for the growth of both the c-GaN and c-InN films, the film's quality is usually degraded by the large difference of lattice constants and thermal expansion coefficients between c-GaN and c-InN film with the substrates. The lattice parameters and coefficients of thermal expansion of III-nitride materials and their substrates are shown in Table 1.1.

Substrate material	Lattice constant (Å)	Lattice mismatch (%)	Thermal expansion coefficient(10^{-6} K^{-1})
c-GaN	4.520 [26]	0	3.17 [27]
GaAs	5.653 [26]	-20.3	6.0 [26]
Si	5.430 [26]	-17.0	3.59 [26]
GaP	5.451 [27]	-17.5	4.65 [27]
3C-SiC	4.359 [27]	3.3	3.9 [27]

Table 1.1: The lattice parameters, lattice mismatch and the thermal expansion coefficients of c-GaN and their possible substrates [26], [27].

Substrate material	Lattice constant (Å)	Lattice mismatch (%)	Thermal expansion coefficient(10^{-6} K^{-1})
c-InN	4.980 [26]	0	3.8 [27]
c-GaN	4.520 [26]	10.7	3.17 [27]
MgO	4.216 [26]	18.3	10.5 [26]
GaAs	5.653 [26]	-11.9	6 [26]
3C-SiC	4.359 [27]	14.2	3.9 [27]

Table 1.2: The lattice parameters, lattice mismatch and the thermal expansion coefficients of c-InN and their possible substrates [26], [27].

1.2 Planar defect in cubic GaN and cubic InN

It is well known that GaN and InN can be crystalized in both cubic and hexagonal structures, which were reported by many research groups, showing the planar defects (stacking faults and twins) generated in the cubic phase structure [28, 29] due to the structural similarities between the cubic (111) and hexagonal (0001) planes. The difference between these two crystal structures is just a 60° rotation along the cubic (111) or hexagonal (0001) surfaces, as shown in Figs 1.2(a) and 1.2(b). According to our previous reports in the case of c-GaN [30, 31] these structural similarities show the possibility that the metastable cubic structure can be easily transformed to be the stable hexagonal structure along the ⟨111⟩ directions of cubic-phase structure.

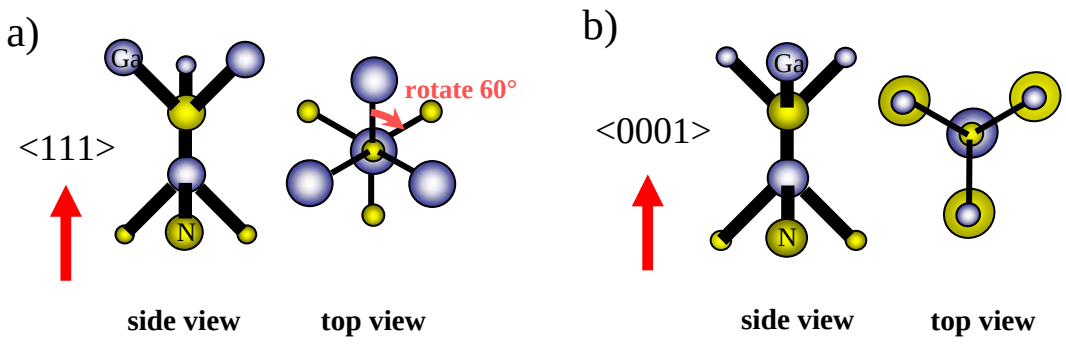

Figure 1.2: Schematic illustrations of GaN structure on side view and top view of, (a) cubic structure along <111> and (b) hexagonal structure along <0001> direction.

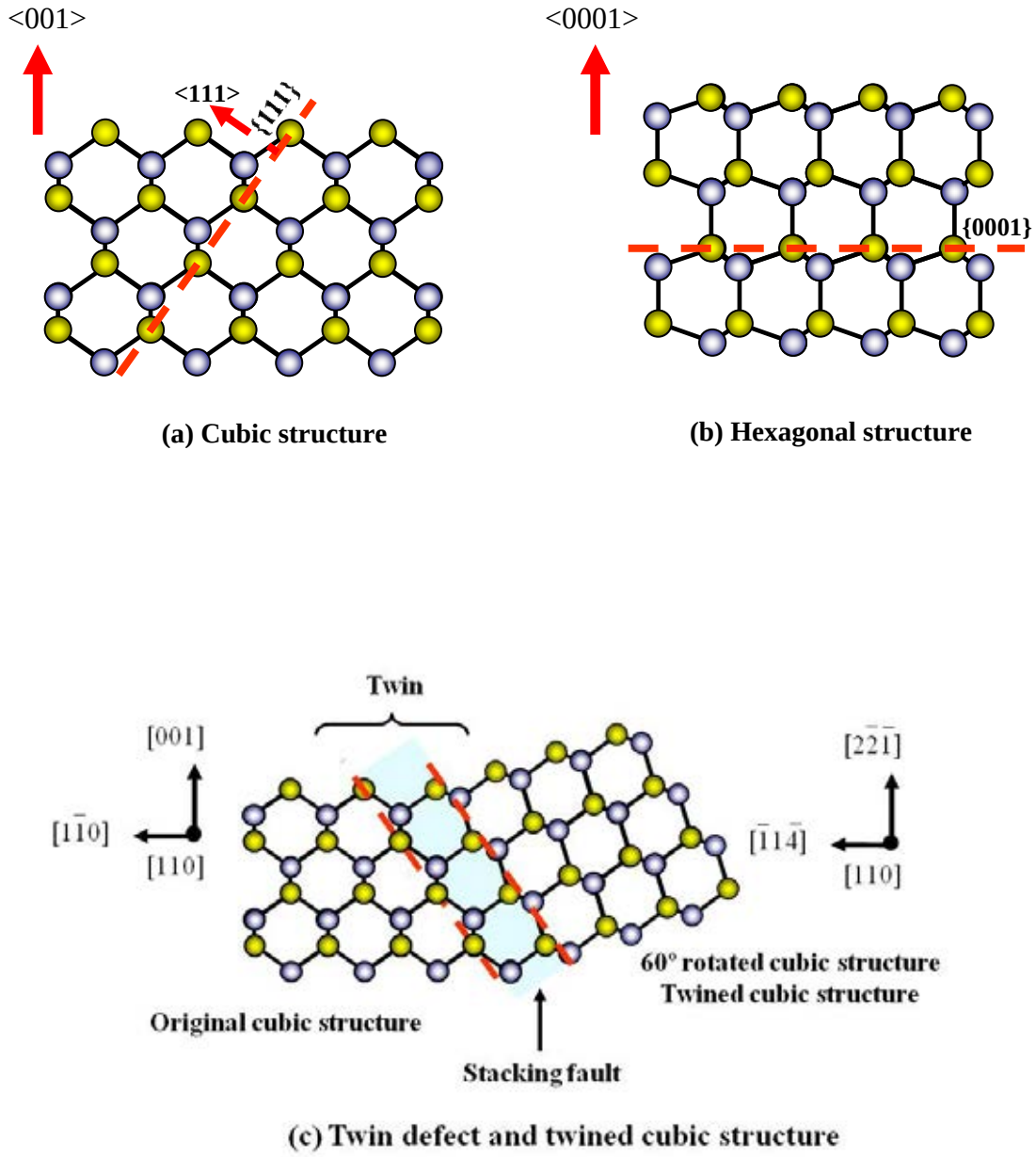

Figure 1.3: Schematic illustrations of 2-dimension GaN structure (a) c-GaN, (b) h-GaN and (c) stacking fault, twin and twined cubic structure.

Thus, the cubic structure of GaN can be mixed with the hexagonal phase in form of planar defects that are stacking faults (SFs) and twins on the (111) planes of the cubic structure. Figures 1.3(a) and (b) respectively show two-dimensional lattice models without planar defect of the cubic structure along the <001> axis and the hexagonal structure along the <0001> axis. A simple two-dimensional lattice model of possible planar defects, such as SFs and twins, are shown in Fig.1.3(c). With this model, planar defects formed by an insertion a 1 monolayer of hexagonal structure on the cubic structure (111) plane, leading to a generation of SFs and twined cubic domain. Thus, the twin defects occur when a mono-layer of hexagonal phase is inserted between two single crystalline cubic structures that make another side of single crystalline cubic structure rotated by 60° leading to the mirror symmetry of c-GaN structure, called twined cubic structure. Since the stacking fault on cubic (111) plane is generated by an insertion of 1 monolayer of hexagonal and stacking fault on hexagonal (0001) plane is also generated by an insertion of 1 monolayer of cubic structure. The mixed hexagonal-phase in cubic-phase structure formed by planar defects, such as SFs and twins, is the major factor, which degrades the crystal quality of the cubic nitride films [32]. In the case of c-InN, the structural defects as observed in the case of c-GaN are expected.

A generation of planar defects, such as SFs and twins, is also affected by the large mismatch of lattice parameters and thermal expansion coefficients between the cubic nitride films (c-GaN and c-InN) and their substrate materials. To provide a high quality c-GaN and c-InN films with low density of planar defects, an appropriate buffer layer and growth condition are required.

In this work, transmission electron microscopy (TEM) was used to analyze the effects of buffer layers that inserted between the cubic nitride film and substrate to achieve the better quality of c-GaN and c-InN. The formation and distribution of extended defects in the c-GaN and c-InN thin films were investigated using analytical TEM techniques.

1.3 Objectives and organization of dissertation

The dissertation is focused on transmission electron microscopy (TEM) analysis of a generation of structural defects, such as stacking faults (SFs), dislocations and hexagonal phase inclusion, in the c-GaN and c-InN thin films grown by MOVPE and MBE, respectively. Effects of buffer layers on the crystal quality of c-GaN and c-InN were investigated using both of cross-sectional bright field (BF) and dark fields (DF) images. Especially, the suitable buffer layer can be used to control the crystal structure and to reduce a generation of planar defects. The information obtained from TEM was verified to establish understanding of structural defect generation in the c-GaN and c-InN films. This is an advantageous data used to improve the growth condition to control the crystal structure phase and to develop the crystal quality of the grown films.

Principle of TEM including the analysis of micrographs obtained from TEM measurements and electron diffraction patterns are described in *chapter 2*.

In *chapter 3*, experiments including the preparation of the thin film specimen for TEM analysis are described in details.

In *chapter 4*, TEM analyses of defect structures in the c-GaN thin films grown with and without AlGaAs buffer layer on GaAs (001) substrates have been reported. Structural phase transition from c-GaN to h-GaN is proposed to form the planar-defects, such as SFs and twins. We found that this is due to an emerging of the (111)-step surface of the AlGaAs buffer layer.

In *chapter 5*, a distribution of structural defects in the c-GaN film grown on GaAs (001) substrate was verified to be affected by an insertion of AlGaAs buffer layer. Two different types of defect structures taken along the [110] and [$1\bar{1}0$] zone axes are verified to be SFs and TDs respectively, indicating defect anisotropic distribution. This is due to an existence of twin and anti-phase boundary in the films, which were clearly observed in cross-section TEM images taken along the [$1\bar{1}0$] zone axis.

In *chapter 6*, TEM analyses of hexagonal-phase generation in MBE grown cubic InN on MgO (001) substrate using a c-GaN buffer layer. Hexagonal structure in c-InN film is propagated from the h-GaN region in the c-GaN buffer layer.

Finally, *chapter 7* gives the conclusion of the dissertation.

CHAPTER II

TRANSMISSION ELECTRON MICROSCOPY (TEM)

2.1 Introduction of TEM

The transmission electron microscopy (TEM) is a powerful instrument that can demonstrate image details down to an atomic level. The wavelength of the electrons in the TEM is ~ 10,000 times shorter than visible light leads to the high resolution of TEM reaching the order of 0.2 nm. Since TEM can form bright field (BF) image, dark field (DF) image and electron diffraction pattern to investigate the microstructure and crystal structure of the material. Moreover, TEM have influenced to study in nano-science and nano-technology; although, equipment operation and result interpretation are complicate leading to limitation of the material investigation by TEM.

2.2 The resolution of TEM

The electron gun is the source of electron beams that are smaller than atoms enabling atomic resolution in material images. According to the classical Rayleigh criterion for light microscopy, a formula of resolutions is given by [33]

$$\delta = \frac{0.61\,\lambda}{\beta} \tag{2.1}$$

where λ is the wavelength of the radiation,

β is the semi-angle of collection of the magnifying lens.

The energy of electron E, is related with the wavelength of electron. The energy of electron is the accelerating voltage of electron gun. Approximate electron wavelength, for a 100 keV, ~ 0.004 nm.

Approximately, is [33]

$$\lambda \sim \frac{1.22}{\sqrt{E}} \tag{2.2}$$

where E is electron volts (eV),

λ is electron wavelength (nm).

The higher resolution obtained by increasing the voltage which is the best way to approach atomic resolution in close-packed structures. Typically, the electron beam energy used in the range from 100-400 keV, which is much smaller than the diameter of an atom.

2.3 The concept of component in TEM

2.3.1 TEM operation using a parallel beam

The TEM consists of the electron gun to produce an electron beam and their energy is typically 100-400 keV. The condenser lens system projects the parallel beam to a specimen lead to coherent as possible which got sharpest diffraction patterns and the best image contrast [34]. The electrons pass through the crystalline specimen which is scattered according to Bragg's law. The transmitted beam is focused by the objective lens to form a diffraction pattern at the back focal plane. To form the image, the diffraction spot must be selected by the objective aperture. The image system lens focused on the first image formed to form a final magnified image on the viewing screen. The schematic illustration of a TEM set-up is showed in Fig.2.1.

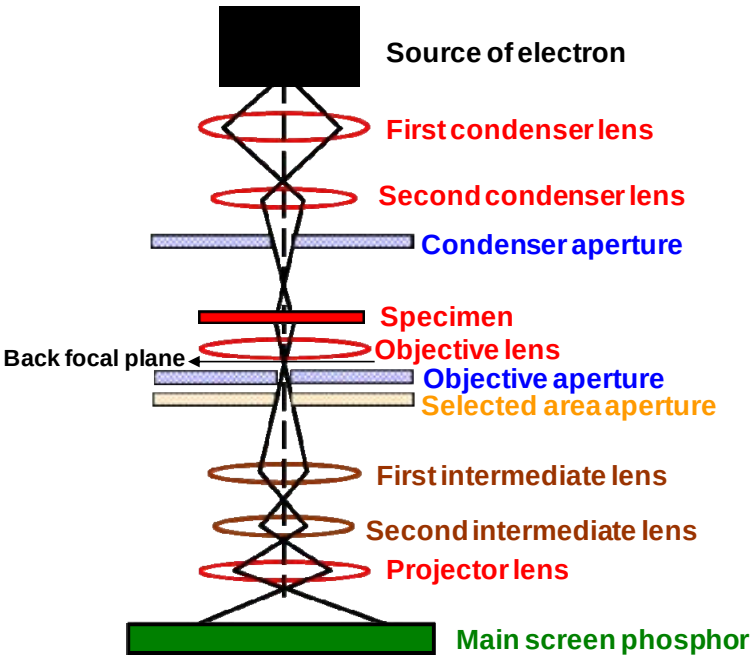

Figure 2.1: The schematic illustration of TEM [35].

2.3.2 Selected Area Diffraction

The selected-area diffraction (SAD) is useful to correlate the morphology and crystallographic information in small specific area of specimen. The SAD aperture inserted into the image plane of the objective lens, which is a means of confining the diffraction pattern from a selected area of the specimen. Therefore, the SAD pattern on the viewing screen originated from the area selected in the image mode.

2.4 TEM imaging mode

The contrast in TEM is generated from a difference in the number of scattered electrons, when they pass through the specimen. Electron scattering from transmitted beam has two mechanisms to form image as mass-density contrast and diffraction contrast.

Mass-Density Contrast: The electrons beam interacted with an atomic nucleus that changes path of electrons due to less mass than an atomic nucleus. The numbers of scattered electron at specific area in specimen depends on the density and thickness at that area. The difference brightness area of image is determined by the intensity of scattered electrons. The intensity of the transmitted beam (I_t) is the intensity of primary beam (I_o) less the intensity of beam diffracted by specimen (I_d) [36]

$$I_t = I_o - I_d \quad (2.3)$$

The contrast (C) in a TEM is defined

$$C = (I_o – I_t)/I_o \quad (2.4)$$

The mass-density contrast is the mechanism for image formation that exists in all types of materials.

Diffraction Contrast: The diffraction contrast is generated before the formation of TEM images. The scattered electrons from crystal planes (hkl) corresponding to Bragg condition that satisfied at certain angles between electron beams and crystal orientation. The diffractions beam is focused on the back focal plane of the objective lens to form a diffraction pattern which consists of a set of diffraction spots belonging to one crystal zone. It is called the zone axis parallel to the transmitted beam. The diffraction contrast can generate the bright field and dark field TEM images by selecting the diffracted spot.

2.4.1 The bright field image and dark field image

The two basic image operations in the TEM perform are bright field (BF) image and dark field (DF) image when the SAD pattern is projected onto the viewing screen. The SAD pattern contains the direct electrons which transmitted from specimen without scattering and scattered electron follow Bragg’s law. The way to form the image in TEM is form by using the central spot or the diffracted electron. An objective aperture is inserted into the back focal plane of the objective lens to block

the rest of diffraction pattern except the spot that wanted to form an image. A bright field (BF) image can be formed by selecting the central spot by the objective aperture as shown in Fig.2.2(a). When a scattered electron is selected to form an image by selecting position of the objective aperture around a diffracted spot to generate a dark field (DF) image as shown in Fig.2.2(b).

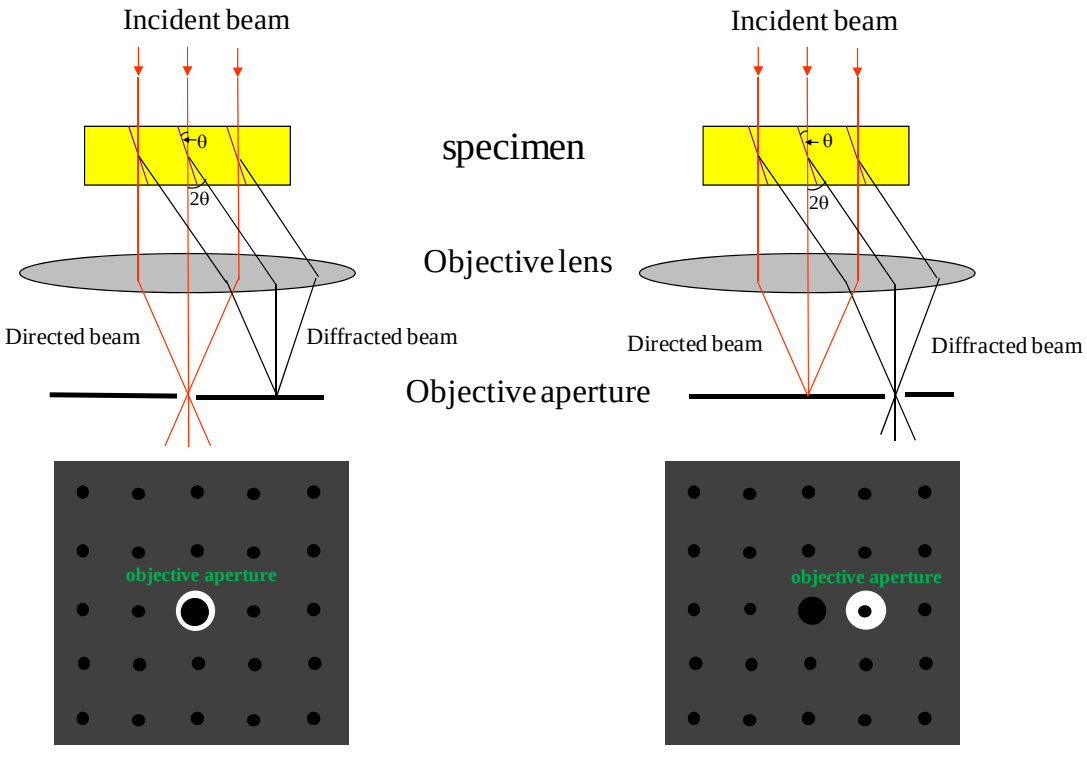

Figure 2.2: The selected area diffraction (SAD) of (a) Bright field image and (b) Dark field image.

2.4.2 Diffraction pattern

The diffraction pattern contains information on the crystal structure, lattice parameter, symmetry, defect and specimen shape. The advantage of TEM, the diffraction pattern can be related to the image of the interesting area.

In crystal, the formation of electron diffraction pattern which diffracted from planes according to Bragg's law. The vector g is vector perpendicular to the reflecting plane {hkl} is called reciprocal lattice vectors. Thus the diffraction pattern contains the vector g lying normal to the electron beam as shown in Fig.2.3.

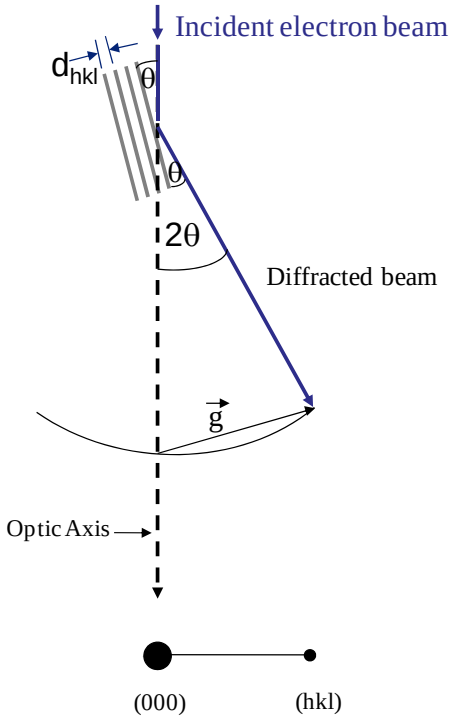

Figure 2.3: Schematic diagram of the formation of a diffraction pattern in the TEM.

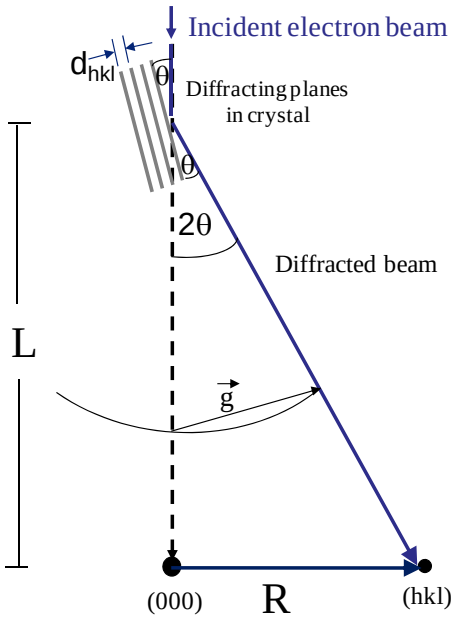

Figure 2.4: Schematic diagram of the effective camera length (L) in the TEM [25].

The magnitude of vector g equal to the reciprocal of the d-spacing of the particular hkl planes involved. From d-spacing of cubic structure

$$d = \frac{a_0}{\sqrt{h^2 + k^2 + l^2}} \tag{2.5}$$

Thus,

$$|g| = \frac{1}{d} = \frac{\sqrt{h^2 + k^2 + l^2}}{a_0} \tag{2.6}$$

Where h,k,l are always integers, identical to the Miller indicies of the reflecting planes. The reciprocal lattice vector g is perpendicular to the real lattice plane (hkl) and is of magnitude $1/d_{hkl}$.

2.4.3 Indexing Diffraction Pattern

The distances measured on the diffraction pattern are actually magnified reciprocal lattice vectors. The magnification factor for the microscope is λL, where L is the effective camera length resulting from the magnifications of the imaging lenses of the microscope column as shown in Fig.2.4. Any distance R is measured from direct beam to the diffraction spot on the diffraction pattern is related to a specific spacing in the crystal (d). Therefore, R = L tan 2θ use the fact that angles are small. It is given R ≈ L sin 2θ = L(λ/d) = R(λL). The last equality,

$$Rd = \lambda L \tag{2.7}$$

which λL is constant.

The ratio between two reciprocal lattice vectors is

$$\frac{R_1}{R_2} = \frac{d_2}{d_1} \tag{2.8}$$

For the cubic system

$$\frac{R_2}{R_1} = \frac{d_1}{d_2} = \frac{\sqrt{h_2^2 + k_2^2 + l_2^2}}{\sqrt{h_1^2 + k_1^2 + l_1^2}} \tag{2.9}$$

where $h_1k_1l_1$ and $h_2k_2l_2$ are the Miller indices of the two diffraction planes from the spot on the diffraction pattern R_1 and R_2.

The steps for indexing diffraction pattern solution are as follows:

1. Measure a distance of diffraction spot from the origin and fine their ratio of R_2/R_1 from the allowed (hkl) of an fcc crystal and compare the ratio with table 2.1.

2. Measure the angle between two reciprocal vector and assigns sign and confirm the position of indices such that the angle is correct. That is,

$$R_1 \bullet R_2 = |R_1||R_2|\cos\theta \tag{2.10}$$

3. A final check is made by the cross product R_1 x R_2, and determines the zone axis of the reflecting planes.

4. Completing the diffraction pattern to the rest of the spots on the pattern.

For example: electron diffraction pattern in the face center cubic (fcc) system taken along the $[1\bar{1}0]$ zone axis.

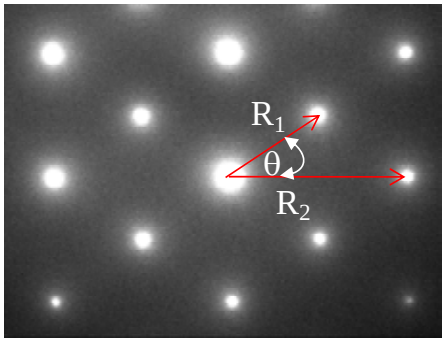

Figure 2.5**:** Diffraction pattern of InN along $[1\bar{1}0]$ zone axis

The ratio of R_2/R_1 from measurement of ED pattern in Fig. 2.5 is about 1.63. The two *d*-spacing ratio shown in Table 2.1 indicates that a first spot and the other spot correspond to {220} and {111} planes, respectively.

		R_1					
R_2	**hkl**	{111}	{200}	{220}	{311}	{222}	{400}
	{111}	1	1.16	1.63	1.91	2	2.31
	{200}	0.87	1	1.41	1.66	2.45	2.83
	{220}	0.61	0.71	1	1.17	1.22	1.41
	{311}	0.52	0.60	0.85	1	1.04	1.21
	{222}	0.50	0.58	0.82	0.96	1	1.15
	{400}	0.43	0.50	0.71	0.83	0.87	1

Table 2.1: The ratio of *d*-spacing ratio for some planes of fcc structure.

To confirm theses results, the angle between both planes, which have been indexed, is examined using the scalar product, as following

$$\vec{R}_1 \cdot \vec{R}_2 = R_1 R_2 \cos\theta, \tag{2.11}$$

so, for [220] and [111] vectors

$$[220]\cdot[111] = \left|[220]\right| \times \left|[111]\right| \cos\theta, \tag{2.12}$$

And check with the measured angle, θ in Fig. 2.5. If the measured angle agrees with the calculate angle, the indexing will be accepted.

In this case, the measured θ is 35.2°, which the calculated θ is 35.26°. It confirms the results of indexing.

2.5 Defect in Thin Film

2.5.1 Dislocations

The crystal line defects are dislocation showing dark lines in the bright field images and bright lines in the dark field images. The electrons of transmitted beam will be diffracted into the diffraction direction which increased diffraction intensity at a portion of the lattice plane. The lattice plane near the core of an edge dislocation is bended lead to a dark image form at point a near the dislocation core as shown in Fig. 2.6.

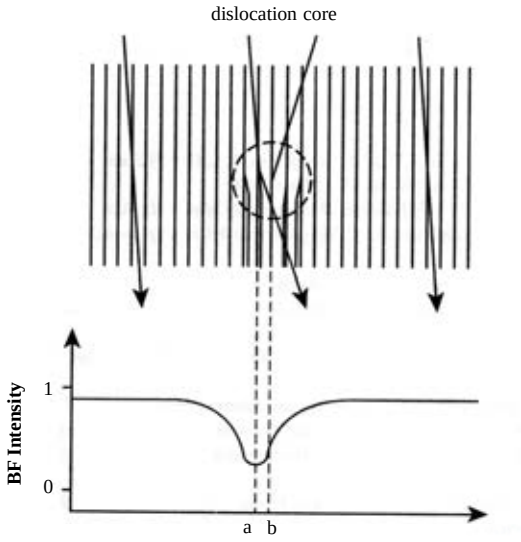

Figure 2.6: Formation of a dislocation image by diffraction beam bend from lattice plane near the core of an edge dislocation [36].

In general, dislocations in semiconductor materials are trap for charge carriers. There are 2 types of pure dislocation as an edge and a screw dislocation.

An edge dislocation: An extra plane of atoms is inserted into the top half of the crystal resulting plane in top side are compressed as shown in Fig. 2.7. This type of dislocation line called an edge dislocation. The direction and the magnitude of dislocation can characterize by the Burgers vector, **b**. For an edge dislocation, the Burgers vector is perpendicular to the dislocation line, which explains in Burgers circuit as shown in Fig.2.7. The Burgers circuit doesn't close complete around the dislocation line. The Burgers vector **b** from the start to the end of circuit is defined as the Burgers vector of the dislocation. If the circuit starts in the lower left side, then moving the vector **b** around the dislocation in a clockwise follows the arrow. The lattice row can count 5 toward the top and 8 across to the right in a clockwise manner. To return the start position, the number of lattice positions is 5 jumps downward, but 7 jumps back to the left to complete. Therefore, a Burgers vector **b** is form to complete the circuit return to start point that is the last segment to complete the circuit of dislocation.

Screw Dislocation: A screw dislocation has its Burgers vector **b** parallel to the dislocation line. The Burgers circuit starts at the lower left side and move 5 jumps upward in clockwise direction. To return the start point move 7 jump to the right and 5 jumps move down. But final 7 move to the left are on a plane behind the start plane due to the crystal planes around the core of screw dislocation form helix. So the Burgers vector **b** to complete the Burgers circuit is perpendicular to the plane lies along z axis which parallel with dislocation line as shown in Fig. 2.8.

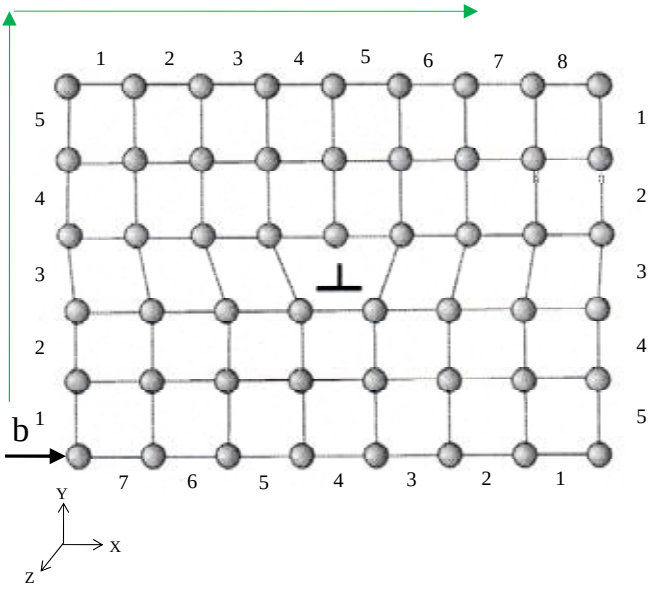

Figure 2.7 The Burgers vector **b** are shown in Burger's circuit for edge dislocation [37].

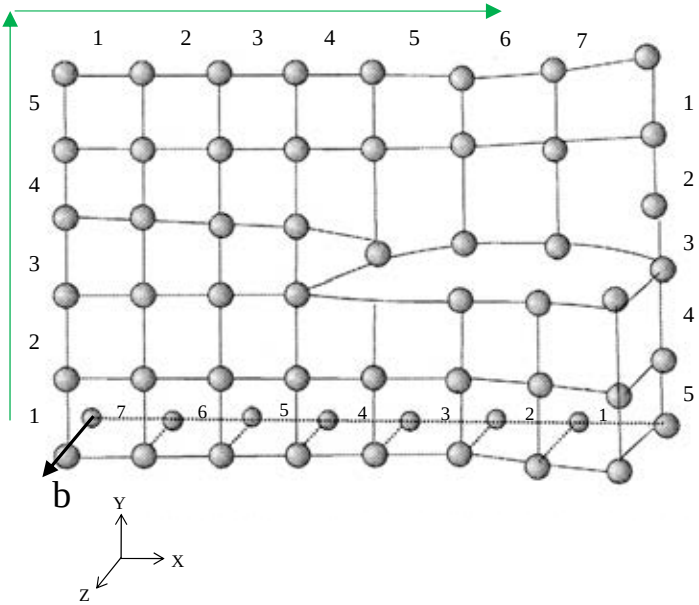

Figure 2.8: The Burgers vector **b** are shown in Burger's circuit for screw dislocation [37].

2.5.2 Planar Defect

Stacking Fault: The stacking sequence in cubic phase structure of the fcc crystal along (111) planes is …ABCABCABCABC…. Stacking faults (SFs) in the cubic phase structure of the fcc crystal occur by insert a layer of hexagonal phase structure (…ABABABABAB…) into cubic phase that is …ABCABCAB│ABCABC…. SFs lie on the {111} planes of cubic phase structure ($\{111\}_{cubic}$) relative with {0001} plane of hexagonal phase structure ($\{0001\}_{hexagonal}$) which parallel with $\{111\}_{cubic}$. The orientation of crystal plane in specimen relate to the electron diffraction pattern. The SFs in cubic phase structure leads to streaks in electron diffraction pattern. These steaks lie on {111} diffraction spots which is normal to the SF planes. Incident beam transmitted through the specimen and consistency of {111} planes of cubic phase structure with SFs lead to streak along the reflection {111} planes as shown in Fig.2.9.

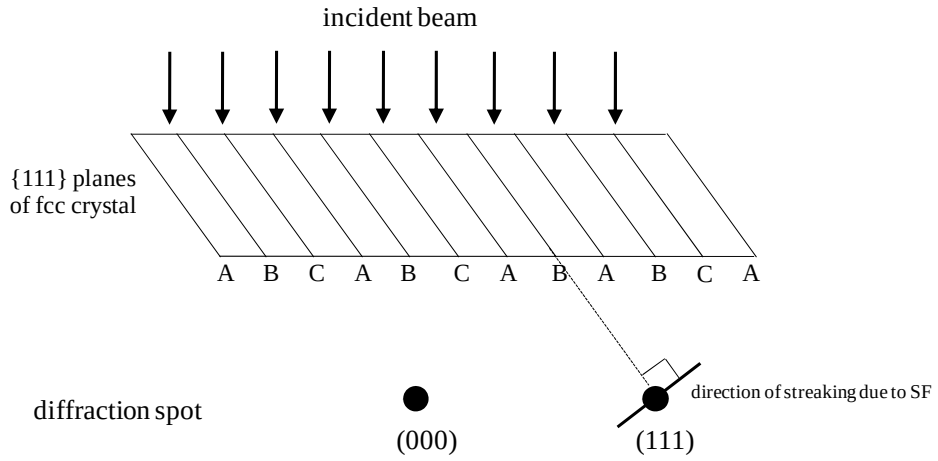

Figure 2.9: Schematic of stacking fault in cubic phase structure lead to streak in (111) diffraction spot.

The diffraction spot of transmitted beam and diffraction spot of (111) plane with streaking are generated in the electron diffraction pattern as shown in Fig. 2.9. The direction of this streak is normal to the SF plan in specimen. Therefore, the streak in electron diffraction pattern along {111} planes can indicate the exits of SFs in specimen.

Twin: The twin region is planar defect in fcc crystal structure which are mirror reflection of crystal structure on the other side. Twining planes in fcc crystal are parallel to {111} plane that is ABCABC|BACBA, with 180° rotation of (111) plane as shown in Fig. 2.10. The twin boundary in the specimen effect their electron diffraction pattern such as leading an extra spot, or increase the intensity of diffraction spot in diffraction spot of the original region. If the twin region is very narrow which transform from original region in cubic phase structure of fcc crystal lead to streak along (111) in electron diffraction pattern [34].

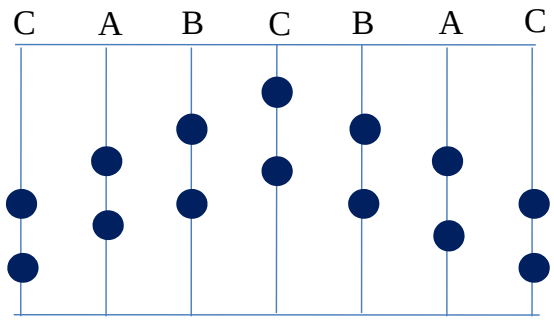

Figure 2.10: Schematic of planar defect as twin in an fcc crystal.

2.6 Double Diffraction

The double diffraction is a phenomenon of which the electron beam is re-diffracted before leaving the specimen resulting in diffraction spot on forbidden position. Most of TEM specimens are thick enough to generate multiple diffraction; where, a very thin of TEM specimen can generate single diffraction [37]. The beam of electrons generates the first diffraction pattern and diffracted beam acts as the incident beam for a second diffraction. The forbidden diffractions are observed in low symmetry such as hexagonal phase. For example, the hexagonal diffraction pattern in $[11\bar{2}0]$ zone axis which the forbidden spots marked with an "X" as shown in Fig. 2.11. For hexagonal crystal the (000l) diffractions are forbidden when l is an odd number. Double diffraction for $[11\bar{2}0]$ zone axis in hexagonal structure show the extra re-flections at {0001}, {0003},… because the combination of any two reflections leads to an existing third reflection [38]. The 0001 reflection in the hexagonal structure is not allowed, but an incident beam along $[11\bar{2}0]$ zone axis of specimen are diffracted by $(1\bar{1}00)$ in the first time and acted as an incident beam and re-diffracted from the $(\bar{1}101)$ planes. This gives $g_1+g_2 = [1\bar{1}00] + [\bar{1}101] = [0001]$ which generated the forbidden diffraction at (0001) plane as shown in Fig. 2.12. For example the other combination of reflections is $[\bar{1}100] + [1\bar{1}01] = [0001]$. The double diffraction in face-centre-cubic (fcc) or body-centre-cubic (bcc) does not exhibit at forbidden location due to allowed reflections generated by a combination of any two diffraction beam [38]. To remove the forbidden reflection due to double diffraction, the specimen is tilted until one of the recombination diffraction beams disappears.

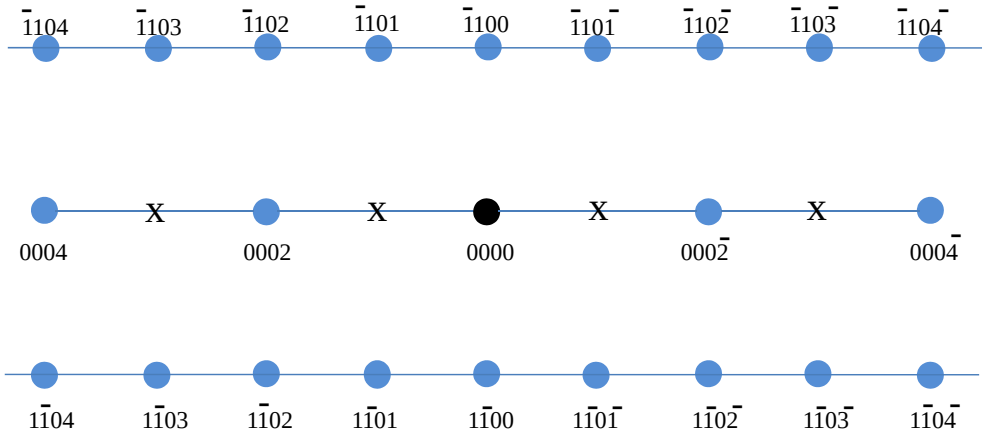

Figure 2.11: Schematic of diffraction pattern of hexagonal structure with forbidden reflection in [11$\bar{2}$0] zone axis.

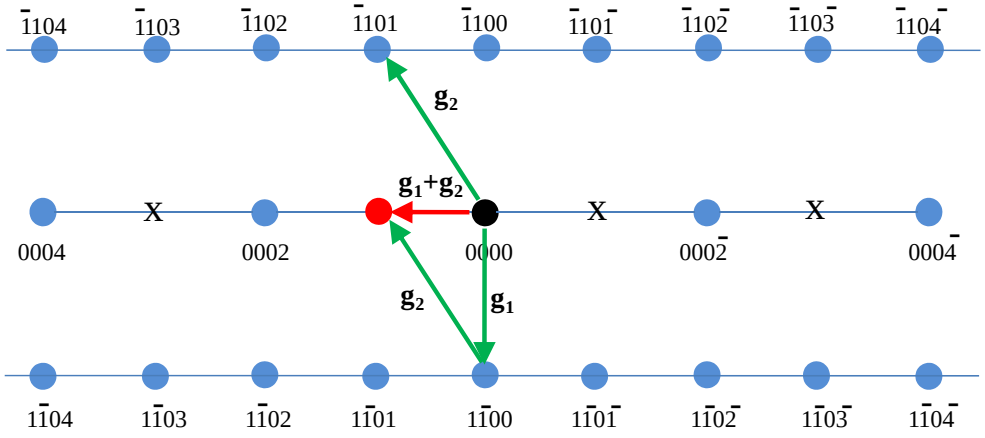

Figure 2.12: Schematic of double diffraction to form forbidden reflection (0001) plane of hexagonal structure in [11$\bar{2}$0] zone axis.

CHAPTER III

EXPERIMENTS

3.1 MOVPE growth of c-GaN films

All c-GaN films were grown on GaAs (001) substrate with and without AlGaAs buffer layer by metal organic vapor phase epitaxy (MOVPE), performing at University of Tokyo, Japan. In this work, TEM has been used to study the effect of AlGaAs intermediate protection layer inserted between GaAs (001) and the low-temperature grown GaN (LT-GaN) at relatively high temperature of 960°C. Comparing with the c-GaN grown directly on the GaAs (001) substrate and c-GaN grown on GaAs/AlGaAs/GaAs (001) substrate. The sample structure used for investigating the effect of AlGaAs buffer layer on c-GaN films is shown in Fig. 3.1.

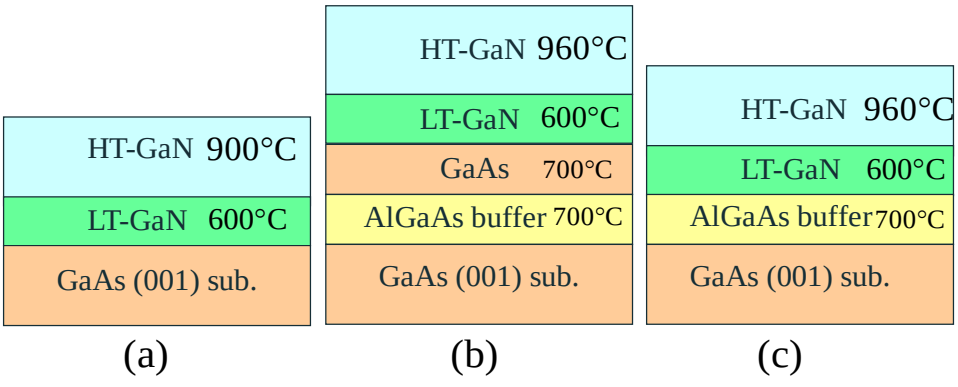

Figure 3.1: Sample structure to investigate the effect of AlGaAs buffer layer on c-GaN film (a) GaN grown without AlGaAs buffer, (b) GaN grown with GaAs layer/AlGaAs buffer and (c) GaN grown with AlGaAs buffer.

The GaN film has been grown on a variety of substrates like sapphire, SiC, Si and GaAs [39, 40]. GaAs substrates are suitable for grown GaN film due to easy to cleave, large wafer size, higher conductivity and similar expansion coefficient to GaN [40, 41]. Moreover this film can be cleaved along with the substrate facet which is easy to prepare laser diodes [19, 39]. The two crystalline structures depend on growth conditions and substrates orientation. Typically, the hexagonal phase (h-GaN) is grown on GaAs (111) and the cubic phase (c-GaN) is grown on GaAs (001) [40, 41]. A problem of GaN on GaAs is that the GaAs substrate is not very stable at high growth temperature due to thermal decomposition of GaAs substrate [42]. Therefore, it is important to protect the substrate from dissociation at high growth temperature for the growth of both h-GaN on GaAs (111) and c-GaN on GaAs (001). The way to protect the surface of GaAs substrate at relatively high growth temperatures is to use buffer layers. Wu et al. [42] grew c-GaN on GaAs (100) substrates at high growth temperature at 980^{o}C by inserting GaN intermediated between the low-temperature grown buffer layer and the high-temperature GaN epilayer to protect the GaAs substrate from thermal dissociation. Recently, there has been a report on the growth of h-GaN on AlAs/GaAs (001) [40, 41, 43]. Despite GaAs and AlAs has almost the same of lattice parameters and zinc-blend structure [43]. It was found that (0001)-oriented h-GaN was grown on GaAs (001) if an AlAs layer is inserted between GaN and the GaAs (001) substrate.

3.2 MBE growth of c-InN films

The c-InN films were grown on MgO (001) substrate with c-GaN buffer layer by molecular beam epitaxy system equipped with a radio-frequency nitrogen plasma source (RF-N_2 plasma MBE), performing at Saitama University, Japan. To clarify the growth temperature and In flux dependence of the quality of c-InN films by changing the growth condition. The sample structure is shown in Fig.3.2.

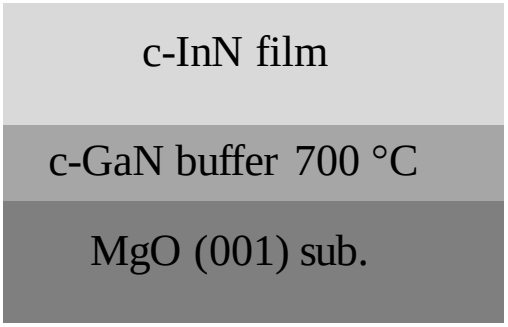

Figure 3.2: The growth condition of c-InN films grown on MgO (001) substrate using c-GaN buffer: growth temperature of c-InN layer sample (a) 500°C with In flux: 8×10^{-5}Pa, sample (b) 475°C with In flux: 8×10^{-5}Pa and sample (c) 475°C with In flux: 4×10^{-5}Pa.

The very smooth surface of c-GaN buffer layer, with a thickness of 400 nm was grown on MgO (001) substrate at 700°C [43]. There is 1-2% of hexagonal phase content in c-GaN buffer layer. Next step, the c-InN layer was grown for 1 hour at 475-500°C with various In fluxes. The In fluxes varied in the range of (4×10^{-5} - 8×10^{-5} Pa). The supplied N_2 flow rate and RF power were 1.6 standard cubic centimeters per

minute (sccm) and 400 W, respectively. According to Y. Iwahashi [44] investigated the influence of growth temperature and III/V ratio on the crystal quality of c-InN film. It was found that the high phase purity and a smooth surface of c-InN film dependent on growth at relative higher temperature and increasing In flux. In this study, the c-InN grown on MgO (001) substrate using c-GaN buffer layer that varied the growth conditions both of growth temperature and In flux to investigate the effect of growth condition on the formation of hexagonal phase inclusion (h-InN) in c-InN films. TEM used to investigate the crystal structure and structural defect of c-InN film grown on MgO (001) substrate by using c-GaN buffer layer which observed on h-InN generated in c-InN films with propagating from hexagonal phase content in c-GaN buffer layer.

3.3 Sample preparation for TEM analysis

The methods of sample preparation for TEM depend on the type of material and the desired information. Cross-sectional TEM images of specimens are suitable for studying the interface and plan-view TEM images of specimens are suitable for surface morphology. Sample preparation for cross-sectional image has to consider the interface is parallel to the electron beam. Therefore, cutting the sample into thin slices normal to the interface using diamond saw. In this study, the GaN grown on GaAs (001) substrate with and without AlGaAs buffer layer can be cleaved with diamond pen. The InN grown on MgO (001) with GaN buffer layer can be cut by a diamond saw. The techniques for preparing cross-sectional specimens are following the steps shown in Fig.3.3. First, the sample is cut 3 mm diameter disk. The surfaces of films

are glued together with M-bond 610 glue to produce the interface like a sandwich and clamp the sample with curing at 170°C around 3-4 hours. The sample is struck on the tri-angle shape of glass holder by Kenji glue, orienting interfaces with M-bond 610 glue normal to the glass holder. The diamond films size of 9, 6, 3, 1 and 0.5 μm used for mechanical polishing for thinning sample by polishing on the polishing wheel.

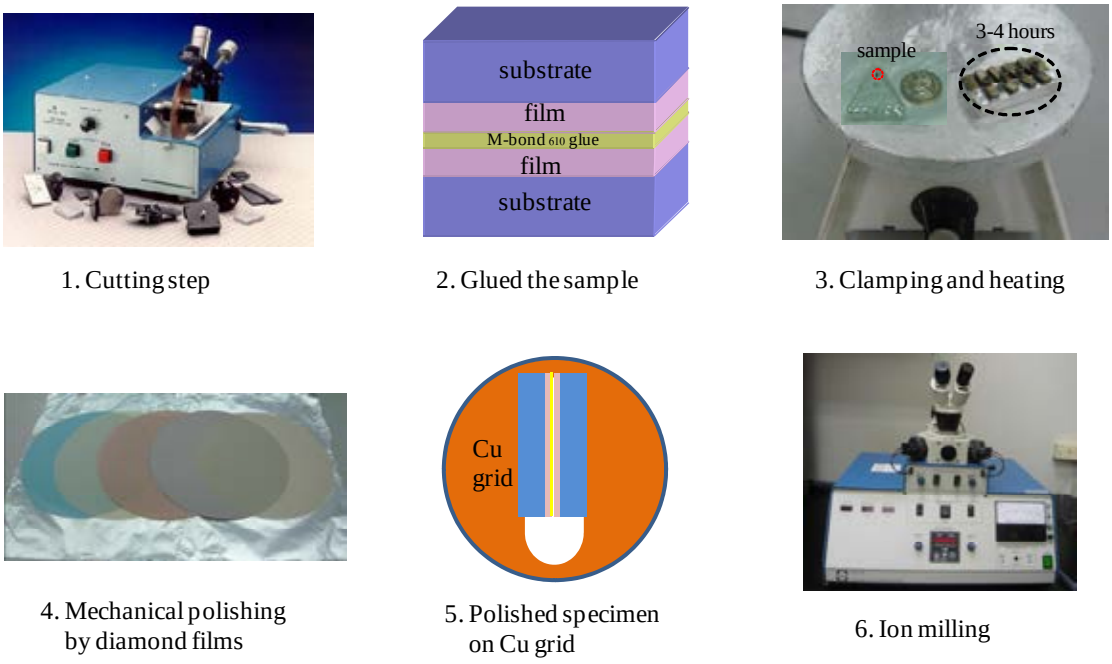

Figure 3.3: The steps of sample preparation for TEM analysis.

At the first side sample, polishing is stopped when size of the sample decreased to a half. Next, polish to the second side, until the sample is thin enough for Ion Milling. The polished sample is supported on Cu grid that has a 3 mm in diameter. Ion milling is used for bombarding the sample with energetic ions, until the sample is thin enough

for studying by TEM. In this study, precision ion polishing system (PIPS) is used for thinning the sample. There are two available ion guns to thin from each side. The PIPS equipment can adjust the thinning parameter as the ion energy, the angles of incidence to thin sample and the rate of sample rotation. This technique is suitable for thermal stable specimen such as metal and ceramics. The energy of ion beam bombards the specimen in a ranged 1- 6 keV depending on thickness of the polished sample. The specimen is placed in the center between two ion guns with adjustable angle of -10 – 10 degrees. Specimen is bombards in large area, if the angle of ion gun is low. On the other hand, if the angle of ion gun is high, specimen is bombards in small area.

3.4 Raman scattering

The molecular vibrations can detect and measured by Raman spectrum with application in gas, liquid or solid sample. In this work, Raman scattering use to analyze the phase of crystal structure which distinguish between different phases in thin film. The laser source induces the vibration in sample by absorption and emission of light. The energy difference between an incident optical photon of frequency $h\nu_{inc}$ and emission of the optical photon $h\nu_{emit}$, corresponding to the phonon vibration in sample. In case of $\nu_{inc} > \nu_{emit}$ called a stokes line and $\nu_{inc} < \nu_{emit}$ for an anti-stokes line. The frequency of emitted light intensity can detect. In this study, the micro-Raman scattering was used at room temperature with the Renishaw Ramanscope RM1000. A 514.5 nm line of an Ar^+ laser is used as a monochromatic high frequency light sources as shown the Raman spectroscopy system in Figure 3.4. The laser beam is focused on

the sample with the spot size of ~ 2μm in diameter. The Raman spectra were obtained in the backscattering geometry z(x,y)z̄ and recorded in the range of 250-800 wave number (cm^{-1}).

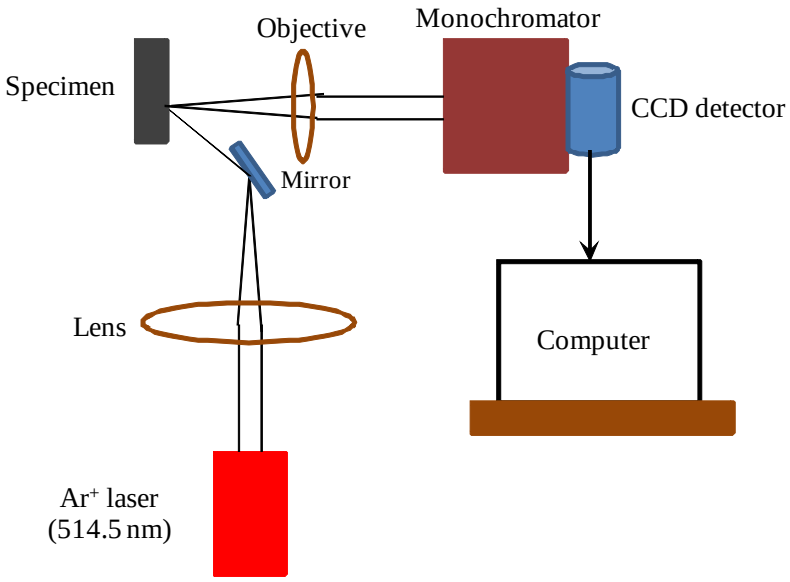

Figure 3.4: Schematic diagram of Raman scattering system.

CHAPTER IV

ANALYSIS OF THE HEXAGONAL PHASE GENERATION IN c-GaN BY USING AlGaAs BUFFER LAYER

4.1 Growth conditions and experiment

GaN samples used in this study were grown on a GaAs (001) substrate in a metalorganic vapor phase epitaxy (MOVPE) system (at the University of Tokyo, Japan) using H_2 carrier gas, at a pressure of 160 Torr. Precursors of Ga, N, Al and As were trimethylgallium (TMGa), 1,1-dimethylhydrazine (DMHy), trimethylgallium (TMAl) and AsH_3, respectively. GaN epitaxial films were grown by a two-stage growth method, which involves the growth of GaN at two substrate temperatures, i.e., the initial growth of GaN at low-temperature (LT-GaN) and subsequent growth of a GaN film at high temperature (HT-GaN), with and without an AlGaAs buffer layer on the GaAs (001) surface. A thick $Al_{0.2}Ga_{0.8}As$ buffer layer around 300 nm and LT-GaN layer were grown at 700 ^oC and 600 ^oC, respectively, followed by the growth of HT-GaN layer at 960 ^oC as showed the sample structure in Fig.4.1(c). For GaN film without an AlGaAs layer buffer growth directly on GaAs (001) substrate was grown at 900 ^oC of HT-GaN as shown in Fig4.1(a). To study the behavior of AlGaAs protect

the GaAs substrate. The GaAs layer grown at 700°C were inserted between LT-GaN and AlGaAs buffer layer as shown in Fig.4.1(b). In order to investigate the effects of the AlGaAs buffer layer on the structural of the GaN films grown on GaAs (001), the 3 sample structures were used to study cross-sectional samples that were prepared using mechanical polishing, and ion polishing down to electron transparency. TEM analysis was performed in JEOL JEM 2010 operating at 200 keV.

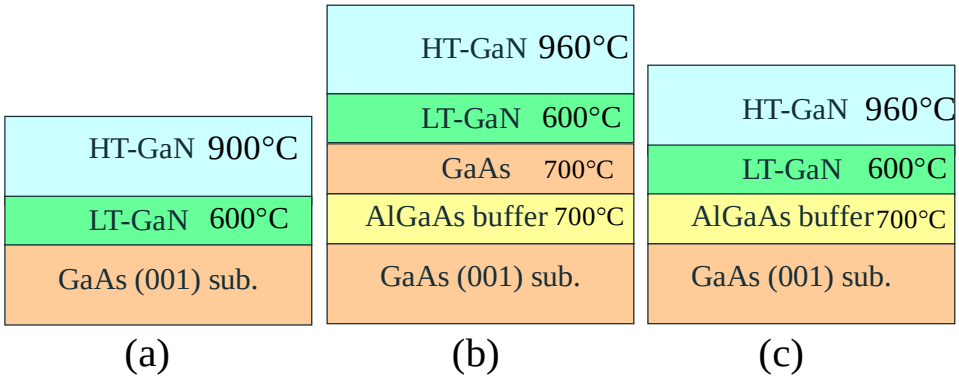

Figure 4.1: Sample structure to investigate the effect of AlGaAs buffer layer on c-GaN film (a) GaN grown without AlGaAs buffer, (b) GaN grown with GaAs layer/AlGaAs buffer and (c) GaN grown with AlGaAs buffer.

4.2 Initial investigation of c-GaN

4.2.1 Cross-sectional morphology

Cross-sectional morphology of GaN films with different sample structure was investigated in micro-scale by scanning electron microscopy (SEM) to provide the initial information of AlGaAs buffer layer effect on GaN sample structure. Figure 4.2 shows the SEM images for the cross-sectional of GaN layer grown on GaAs (001) substrate (a) without and (c) with AlGaAs buffer layer and (b) with GaAs/AlGaAs buffer layer to investigate the AlGaAs buffer layer protect GaAs substrate lead to without voids at the surface of GaAs substrate. For GaN film grown directly on GaAs substrate as shows in Fig. 4.1(a) and 4.2(a) the interface is generally smooth, but displays a pattern of small voids in form of tri-angle shape, which formed as a result of the dissociation from GaAs (001) substrate at high growth temperature (900 °C). In contrast, for the GaN film with the AlGaAs buffer layer grown at higher temperature (960 °C), the interface between the GaN layer and AlGaAs/GaAs(001) substrate is very smooth without any voids as shown in Fig. 4.2(c). Therefore, a higher-quality GaN epitaxial film can be obtained on the GaAs (001) substrate with the assistance of the AlGaAs buffer layer. To study the behavior of AlGaAs buffer layer protected the GaAs substrate from the high temperature. We inserted another GaAs intermediate layer between the AlGaAs buffer layer and the LT-GaN layer, as shown in Fig. 4.1(b) and 4.2(b). It is clearly seen that voids are located only in the GaAs intermediate layer which cannot penetrate to the GaAs substrate due to AlGaAs protection. The area of the voids is expanded in rectangular shape with increasing the temperature at 960 °C. This result can imply that voids stopped on the top of AlGaAs buffer layer and

expanded an area on their lateral. According to cross-sectional SEM image found briefly that the role of AlGaAs buffer layer can protect the GaAs substrate from thermal decomposition showing without voids. The effect of AlGaAs buffer layer on the GaN film was investigated in nano-scale by TEM to study the crystal structure and structural defect of GaN film.

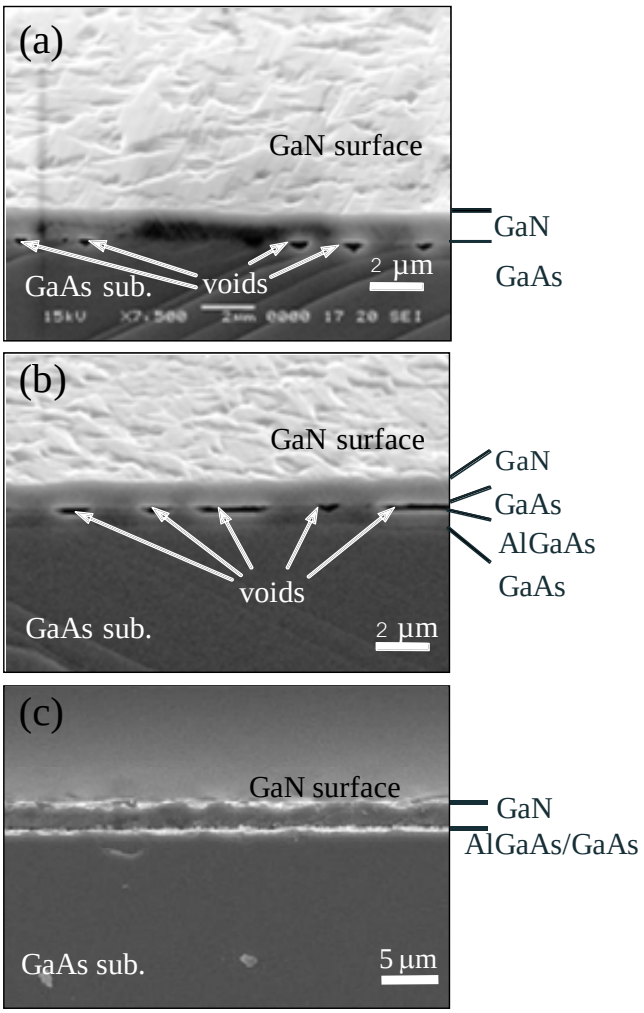

Figure 4.2: Cross-sectional SEM images of the top and cleaved surfaces of GaN layer grown on GaAs (001) substrate (a) without, (c) with the AlGaAs buffer layer and (b) with the GaAs/AlGaAs buffer layer.

4.2.2 Luminescence properties

Luminescence properties of GaN film grown without and with AlGaAs buffer were investigated by photoluminescence (PL) at low temperature. Figure 4.3 shows 5.5 K PL spectra of GaN films grown (a) without and (b) with the AlGaAs buffer layer at temperature of 900 °C and 960 °C, respectively. For the GaN film without the AlGaAs buffer layer, the PL spectrum exhibits the excitonic transition of c-GaN at 3.267 eV [19, 20, 45] with the full width at half maximum (FWHM) as 15 meV, that is very strong compared with the donor-acceptor pair transition at 3.155 eV. Moreover, the PL spectrum exhibits no emission signals above 3.30 eV that corresponds to h-GaN, indicating relatively high purity of c-GaN. For GaN film with

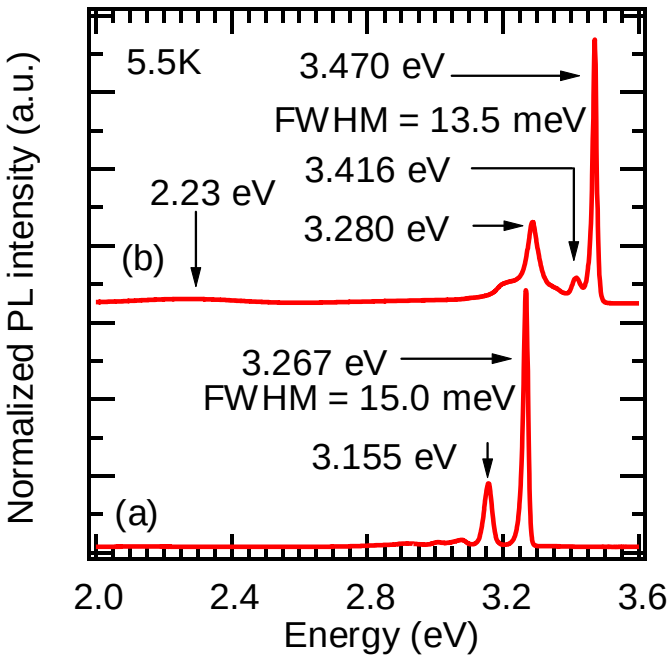

Figure 4.3: Low-temperature (5.5 K) PL spectra of GaN films grown (a) without and (b) with the AlGaAs buffer layer.

the AlGaAs buffer layer, the PL spectrum showed the dominated peak of h-GaN at 3.470 eV that is known as I_2 [19, 38] and the 3.41 eV band [19]. At low energies, contributions of donor-acceptor pair transition (DAP) at 3.28 eV can be seen. This result reveals that the AlGaAs buffer layer affects crystalline orientation having a mixture of h-GaN and c-GaN phases where c-GaN reduces when the AlGaAs buffer layer is inserted.

4.2.3 Vibrational properties

Vibrational properties of GaN film grown without and with AlGaAs buffer layer were investigated by Raman measurement at room temperature. Figure 4.4 showed the Raman spectra that were measured GaN sample at room temperature a) without and b) with the AlGaAs buffer layer. In case of GaN film without AlGaAs buffer layer, transverse-optical (c-TO) phonons and longitudinal-optical (c-LO) phonon of cubic GaN are found at 555.31 cm^{-1} and 737.16 cm^{-1}, and E_2 peak of hexagonal GaN are found at 567.04 cm^{-1}. The c-GaN grown without AlGaAs buffer layer is interfered by hexagonal phase of GaN film and these hexagonal inclusions are too small to be detected by PL measurement. For the GaN film with the AlGaAs buffer layer, the cubic GaN peak is found at 556.48 cm^{-1} (c-TO) and 737.16 cm^{-1} (c-LO), the A_1(TO) peak (hexagonal phase) at 535.36 cm^{-1} and E_2 peak at 567.04 cm^{-1}. From the Raman spectrum, the GaN layer grown on the GaAs (001) substrates without AlGaAs buffer layer consists of both cubic phases and hexagonal phase whereas no emission of the hexagonal phase was detected from the PL measurement, implying that the hexagonal phase was too small to be detected by PL. According to

Suandon et al. [19], they concluded that the hexagonal phase depended significantly on the growth temperature. In fact, more than 85% of cubic phase was achieved for the c-GaN film grown at 900 °C. When the growth temperature increased up to 960 °C, the hexagonal phase is more than 40% at high growth temperature grown c-GaN film, but is less than 15% for the low growth temperature of 900 °C. The crystal structure of GaN film without and with AlGaAs buffer layer were investigated by PL and Raman measurement which found the effect of AlGaAs buffer layer inserted to protect GaAs substrate leading to mixed phase between c-GaN and h-GaN. Therefore, TEM was used to understand the hexagonal phase inclusion in c-GaN film.

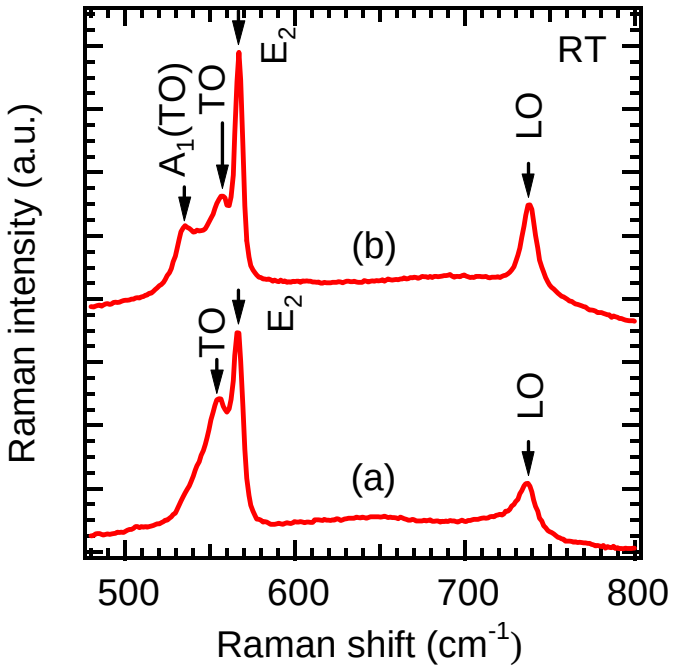

Figure 4.4 Room temperature Raman spectra taken from GaN film grown (a) without and (b) with the AlGaAs buffer layer.

4.3 Analytical TEM: Effects of AlGaAs buffer layer

The effects of AlGaAs buffer layer with c-GaN grown on GaAs (001) were investigated by TEM to study the crystal structure and structural defect. The cross-sectional TEM images taken along [110] zone axis of c-GaN layer grown directly on GaAs (001) substrate as shown in Fig. 4.5(a) without and Fig. 4.5(b) with GaAs/AlGaAs buffer layer to compare the effect of AlGaAs buffer layer that protect the GaAs substrate from thermal decomposition at relatively high growth temperature. For GaN film grown directly on GaAs as shows in Fig. 4.5(a), the interface is generally smooth, but displays a pattern of small voids, which formed as a result of the dissociation from GaAs (001) substrate at high growth temperature (900°C) showing (111) facet. It is known that As removal occurs when the GaAs is exposed to the high temperature and hence the surface becomes very rough promoting creation of voids. The SAD pattern showed the pattern of single c-GaN without streaking in the pattern due to without SFs as shown in Fig.4.5(a). The confirmation of AlGaAs buffer layer can protect the GaAs substrate from thermal decomposition by inserted other GaAs layer for study the behavior and study the role of AlGaAs buffer layer. The cross-sectional TEM image taken along [110] zone axis of c-GaN grown on GaAs/AlGaAs/GaAs (001) substrate as shown in Fig.4.5(b). It is clearly seen that voids located only in the GaAs intermediated layer and the area of voids expanded with increasing the temperature at 960°C. It is evidenced that all the voids

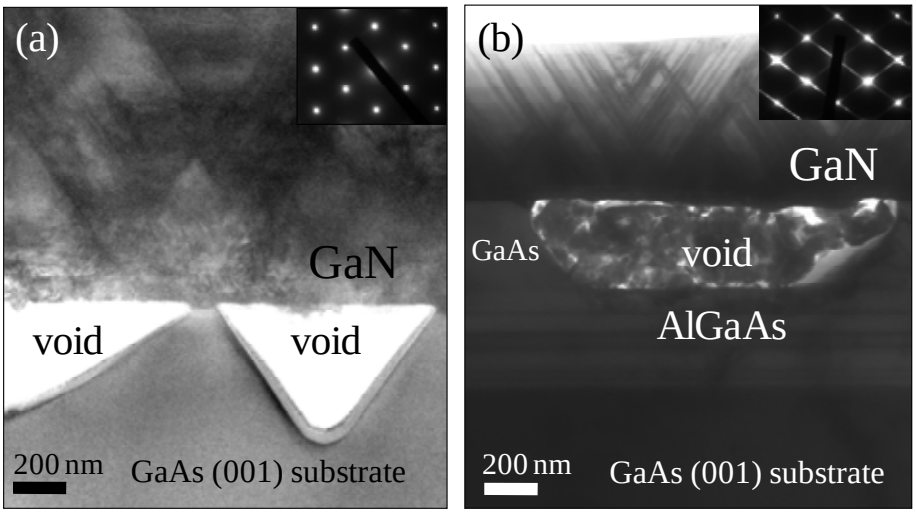

Figure 4.5: Cross-sectional TEM image taken along [110] zone axis and ED pattern of c-GaN (a) without AlGaAs buffer layer and (b) with GaAs/AlGaAs intermediate layer.

were stopped at the top of the AlGaAs surface and hence cannot penetrate into the GaAs (001) substrate. These results indicate that, at higher growth temperature (960°C), the AlGaAs buffer layer plays an efficient role in the protection of GaAs (001) substrate from thermal decomposition. The bright field cross-sectional TEM image show stacking faults (SFs) in plane showing (111) facet of c-GaN as shown in line contrast with 54.7° resulting in streaking of diffraction spots on the SAD pattern.

The bright field cross-sectional TEM image taken from [110] zone axis of the GaN layer grown on GaAs (001) substrate with AlGaAs buffer layer showed in Fig.4.6(a) that studied the effect of AlGaAs buffer. It is seen that characteristic pyramid-like structures generated at interface of GaN film/AlGaAs buffer showing (111) facets at the interface and penetrating into the GaN layer. The SAD pattern in [110] zone axis demonstrates both cubic phase pattern and mixed with hexagonal

phase pattern that govern in the grown layer indicating the incorporation of single crystal h-GaN in the c-GaN layer as shown in Fig.4.6(b). This indicates that the phase transition from cubic to mix phase cubic/hexagonal phase in a form of pyramid-like structure. The diffraction spot indices are shown in fig.4.6(c), 4.6(d) and 4.6(e) showing the epitaxial relationship between the c-GaN and hexagonal incorporation which were found to be c-{111}//h-{0002} and c-<110>//h-<11$\bar{2}$0>.

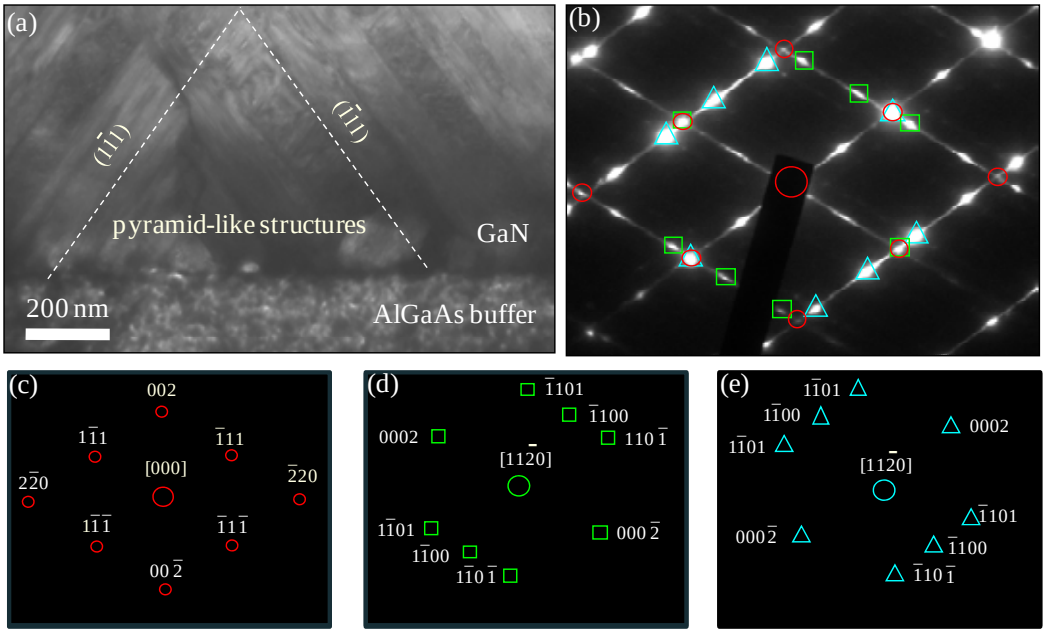

Figure 4.6: Cross-sectional TEM image taken along the [110] zone axis show (a) bright field TEM image of high temperature growth (960°C) GaN layer with AlGaAs buffer layer, (b) corresponding ED pattern of GaN layer, (c), (d) and (e) showing schematic representations of cubic and hexagonal phase related diffraction spots, respectively.

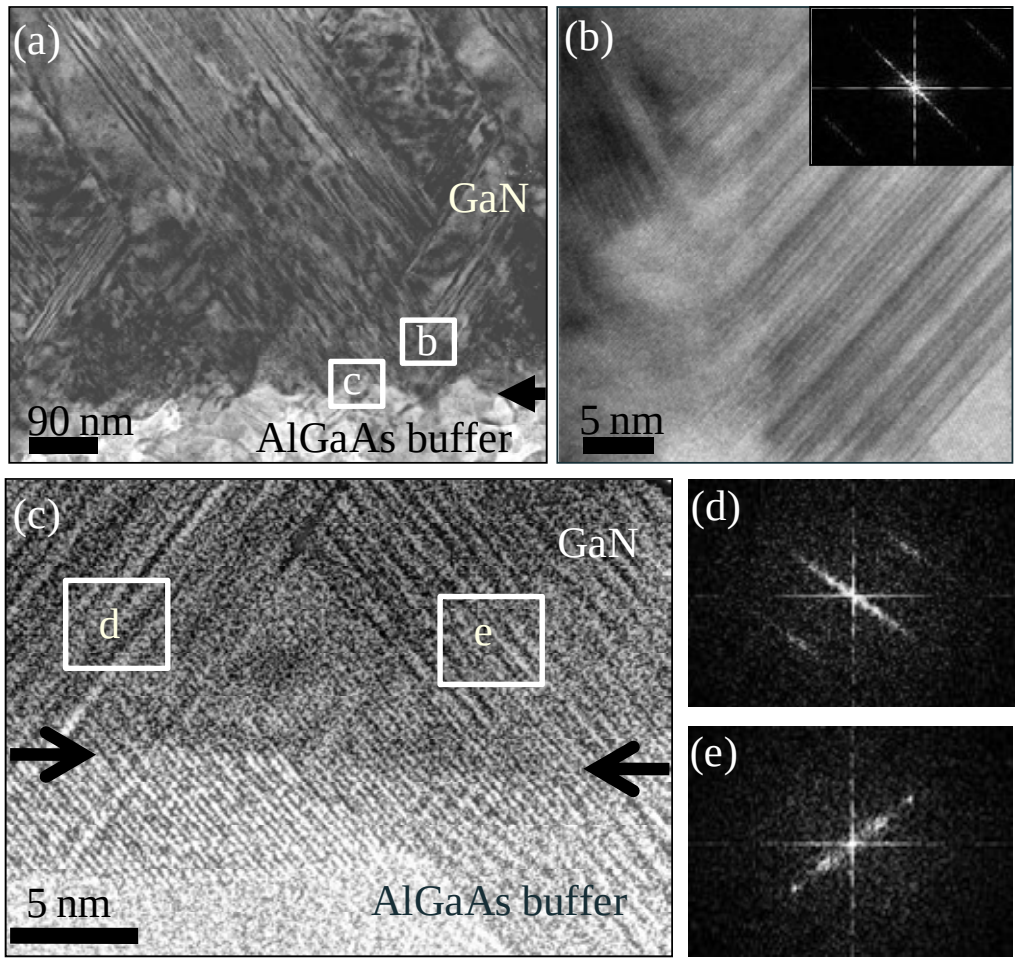

Figure 4.7: Cross-sectional TEM image of (a) interface between GaN/AlGaAs, (b) the HRTEM of planar defect with FFT, (c) the HRTEM taken from interface area between GaN film/AlGaAs buffer, (d) and (e) FFT image of the planar defect.

The higher magnification TEM image obtained from the region of the GaN layer containing the pyramid-like structure that formed in some straight contrast lines. These line contrasts are parallel to {111} plane of c-GaN, identified as planar defect e.g. stacking faults (SFs) and twins. These planar defects often interact with one another and stop their propagation within the layer. But some parts of the planar

defects extend throughout the layer. From TEM images found high density of planar defects that observed at the GaN layer and generated from the rough interface between GaN/AlGaAs buffer layer as shown in Fig.4.7(a). The interface of GaN/AlGaAs demonstrated the roughness leading to (111) step of surface on the (001) AlGaAs buffer layer that originated the planar defects due to atomic surface (111) can generate SFs. The AlGaAs buffer layer inserted to protect the GaAs substrate lead to phase transition from cubic phase to mixed cubic/hexagonal phase that proposed inform of planar defect such as SFs and twins.

Figure 4.7(b) showed high-resolution TEM (HRTEM) image that was taken from square area b of Fig. 4.7(a) containing the planar-defect. This image indicated the cubic phase transition to hexagonal phase along the {0001} planes of hexagonal phase that parallel to the {111} planes of cubic phase. It can confirm that the hexagonal phase incorporation in the cubic phase though the defect on the c-GaN {111} planes to be planar defect. And the Fast Fourier Transform (FFT) image obtained from this planar defect region showing streaks which run normal to the planar defect in corresponding area.

The HRTEM image taken from square area c in the Fig.4.7(a) at the interface area of GaN/AlGaAs as shown in Fig.4.7(c). It is demonstrated the planar defect generated continually from AlGaAs buffer layer to GaN layer. These SFs interact with one another and stop their propagation in the c-GaN layer. The FFT image taken from square area d and e containing the SFs in the Fig. 4.7(c), show streaking run normal with the spot of cubic phase pattern in plane $(1\bar{1}1)$ and $(\bar{1}11)$ due to SFs of GaN layer as shown in Fig.4.7(d) and Fig.4.7(e).

From cross-sectional TEM image and SAD pattern of GaN film with AlGaAs buffer layer are found high density of planar defect that proposed in form of planar defect. The planar defects were suggested to become seeds of hexagonal phase since the growth of GaN on {111} facets or dense of stacking faults could lead to formation of hexagonal phase [46]. Figure 4.8 shows the structural model of atomic configuration when the cubic phase transition to the hexagonal phase along the {111} planes of cubic phase as demonstrated in GaN film with AlGaAs buffer. The cubic structure are metastable compared with hexagonal structure since the cubic structure has ABCABC… stacking sequence along the <111> directions which easily collapses and change to hexagonal structure ABAB… sequence along its <0001> directions [47]. In order to identify the layer stacking sequence of this structure, the periodic structures are located at the cubic structure grown in [001] direction and transform to be hexagonal structure along (111) facet of c-GaN. Due to the {111} surfaces of cubic structure is equivalent to the {0001} surfaces of hexagonal structure.

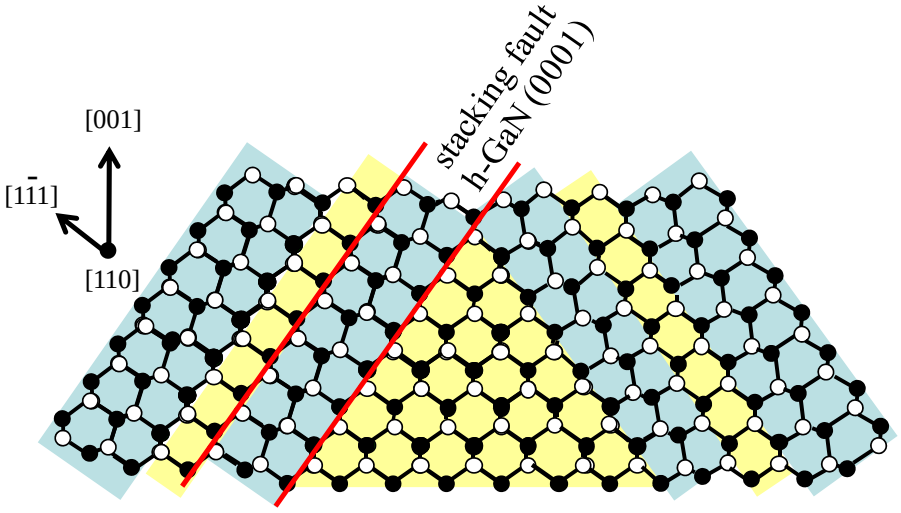

Figure 4.8: Model of atomic configurations of c-GaN is transition to be h-GaN though planar defect along the (111) surface plane of c-GaN.

4.4 Summary

The effect of AlGaAs buffer layer on the epitaxial growth and properties of GaN films on the GaAs (001) substrates have been investigated. From SEM and TEM micrographs, the interfaces between the GaN layer and the layer underneath can be significantly improved with the assistance of AlGaAs buffer layer. The GaN layer grown on AlGaAs buffer layer showed an excellent interface without any voids despite growth at higher temperature (960°C). However, it was found that using the AlGaAs buffer layer lead to structural phase transition from cubic to mix cubic/hexagonal phases as observed from PL and Raman measurements. The phase transition from c-GaN to h-GaN was proposed to occur form planar defects e.g. stacking faults and twins along the (111) surface plane of the c-GaN. From cross-sectional TEM image and ED pattern of GaN with AlGaAs buffer layer are found high density of SFs generated from interface lead to single hexagonal phase GaN mixed in cubic GaN. Therefore, hexagonal GaN mixed in c-GaN film can be grown on {111} surface plane of cubic GaN in form of planar defect such as SFs and twin. Cross-sectional TEM image showing (111) step surface of AlGaAs buffer which can originated the planar defect from interface of GaN/AlGaAs buffer.

Therefore, an improvement of the growth conditions of AlGaAs buffer layer to increase the flatness of surface should be decrease the planar defects such as SFs and twins, which were generated at interface between c-GaN and buffer layer.

CHAPTER V

ANALYSIS OF THE ANISOTROPIC DEFECT IN c-GaN BY USING AlGaAs BUFFER LAYER

The AlGaAs buffer layer was successfully to protect the GaAs (001) substrate from thermal decomposition at high growth temperature (960°C) as showed in cross-sectional TEM image taken along [110] zone axis. There is no voids at the surface of GaAs (001) substrate, however, AlGaAs buffer layer affected on phase-transition of c-GaN layer to mix phase c-GaN/h-GaN though planar defect such as stacking faults (SFs) and twins. High density planar defect constructed in form pyramid-like structure that generated from interface between c-GaN and AlGaAs buffer layer. Due to the roughness of AlGaAs surface act like (111) surface step leading planar defect generated along the (111) surface plane of the c-GaN. Two different types of defect structure which are stacking faults and threading dislocations (TDs) showing defect anisotropic distribution. Cross-sectional TEM images taken along the [110] zone axis showed a high - density of planar defects generated from the interface of GaN/AlGaAs. On the other hand, plan-view image shows that the planar defects are elongated along the [110] direction, but stacking faults are not observe along the $[1\bar{1}0]$ direction. This result was confirmed by the DF TEM images taken along $[1\bar{1}0]$ zone axis, which found a twin boundary along $[\bar{1}1\bar{4}]$ zone axis and APB in c-GaN layer.

5.1 Observation of structural defect distribution

Plan-view TEM image used to study the characteristic of SFs in samples as Fig.5.1 that showed planar defect (SFs) are elongated along the [110] direction, but SFs are not observe along the [1$\bar{1}$0] direction. Electron diffraction pattern of plan view showed the single phase of c-GaN in [001] direction. In general, the type, density and arrangement of a low and moderate SFs density in thin film can use plan-view TEM image to study. But a high density SFs can be studies by cross-sectional TEM image due to the overlapping of SFs contrasts in plan-view image [48]. The plan-view image as Fig.5.1(a) showed the only line contrasts along the [110] direction corresponding with previous observation that found high density of planar defect taken along [110] zone axis from cross-sectional TEM image. A model of defect distribution in c-GaN with AlGaAs buffer layer along [1$\bar{1}$0] zone axis that expected to have a less SFs and appear a horizontal line as showed in Fig.5.1(b). Due to the cross-sectional TEM image taken along [110] showed a high density of SFs parallel to (111) facet of c-GaN and the top-surface made from the top of facet parallel to (111) of c-GaN. Therefore, the anisotropic of planar defect between [110] and [1$\bar{1}$0] can be expected from plan-view image which correspond with cross-sectional TEM image. From plan view TEM image, we can expect the defect in cross-sectional TEM image along [1$\bar{1}$0] zone axis that should be have less planar defect due to no contrast line in this direction.

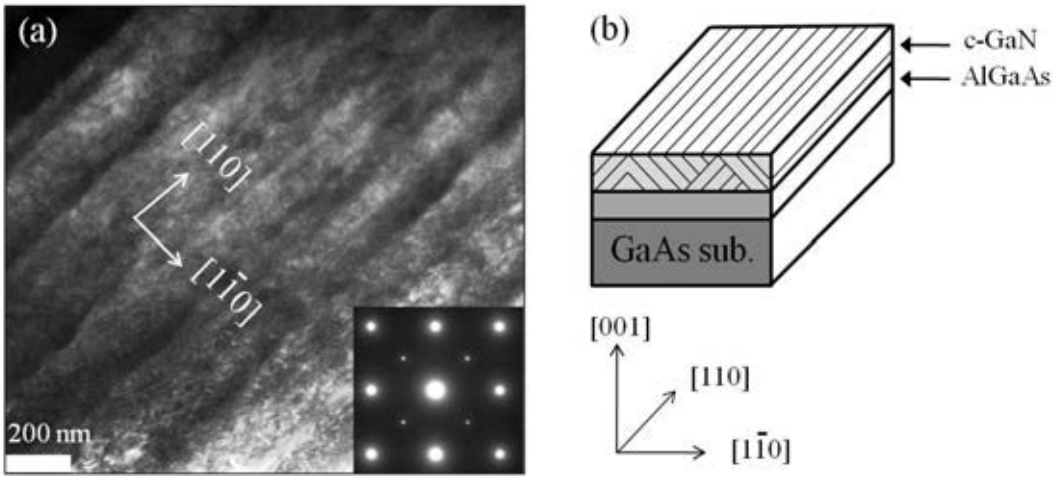

Figure 5.1: (a) plan-view TEM image of c-GaN grown on AlGaAs buffer layer/GaAs (001) substrate showing SFs along [110] direction. Inset shows electron diffraction pattern taken from the sample and (b) the model of defect structure in c-GaN with AlGaAs buffer layer/GaAs (001).

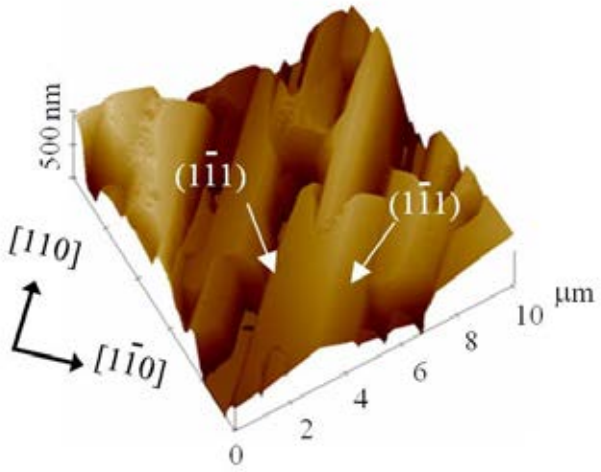

Figure 5.2: Surface morphology of c-GaN/AlGaAs/ GaAs (001) substrate was observed from AFM image.

Atomic Force microscopy (AFM) image of c-GaN/AlGaAs/GaAs (001) substrate were observed the surface of c-GaN as shown in Fig.5.2. The surface morphology of

the GaN film shows the oriented rectangular morphology along [110] direction corresponding with SFs in plan-view TEM image showing the (111) facet of c-GaN that made from the top-surface of SFs.

5.2 Anisotropic distribution of structural defects

5.2.1 Identification of structural defects

Cross-sectional TEM image taken along [1$\bar{1}$0] zone axis to compare the defect structure in [110] zone axis that focused at the interface of c-GaN grown on AlGaAs buffer layer/GaAs (001) substrate was showed in Fig.5.3. The interface of GaN and AlGaAs/GaAs (001) substrate was fairly flat, uniform and no void at the surface of GaAs (001) substrate to confirm the AlGaAs buffer protect GaAs substrate from thermal decomposition. The surface of AlGaAs buffer layer taken from [1$\bar{1}$0] zone axis was smooth leading to defect less in GaN layer. Planar defect e.g. SFs and twins were not found in this region of c-GaN layer and a few threading dislocation originated from interface of c-GaN and AlGaAs buffer layer which differ from defect in [110] zone axis .

To compare the different defect structure between [110] and [1$\bar{1}$0] zone axis showed in Fig.5.4(a) using a dark-field cross-sectional TEM image taken from plane ($\bar{2}$20) of c-GaN grown on AlGaAs/GaAs (001) substrate along [110] zone axis.

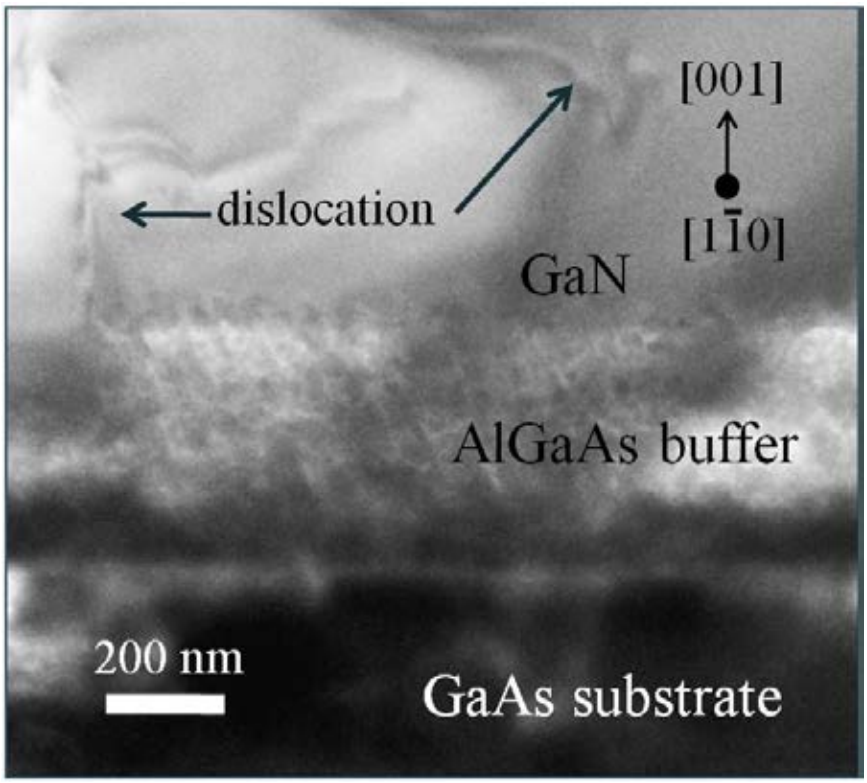

Figure 5.3: Cross-sectional TEM image of c-GaN grown on AlGaAs buffer layer/GaAs (001) substrate taken along [1$\bar{1}$0] zone axis.

The pyramid like structure was demonstrated that constructed in form of planar defect, such as stacking faults, twins and hexagonal phase inclusion, generated along the c-GaN (111) facet. The bright contrast represent the cubic phase from ($\bar{2}$20) plane of GaN which is above the pyramid-like structures indicating the density of SFs decreased from interface of GaN/AlGaAs buffer. In Fig.5.4(b), the electron diffraction pattern showed the mixed phase of cubic structure (red-circle) and hexagonal structure (the white arrow). Therefore, cross-sectional TEM image of GaN grown on AlGaAs buffer on GaAs (001) showed the anisotropic of defect in [110] and [1$\bar{1}$0] zone axis. From the interface between GaN layer and AlGaAs buffer layer as showed

in cross-sectional TEM image taken along [110] showing (111) facet lead to induce the SFs and hexagonal phase growth in c-GaN film. SFs are anisotropic between two [110] and [1$\bar{1}$0] zone-axis because anisotropy of surface morphology that showed (111) surface steps on AlGaAs buffer layer at [110] zone axis lead to the formation seed of SFs [49].

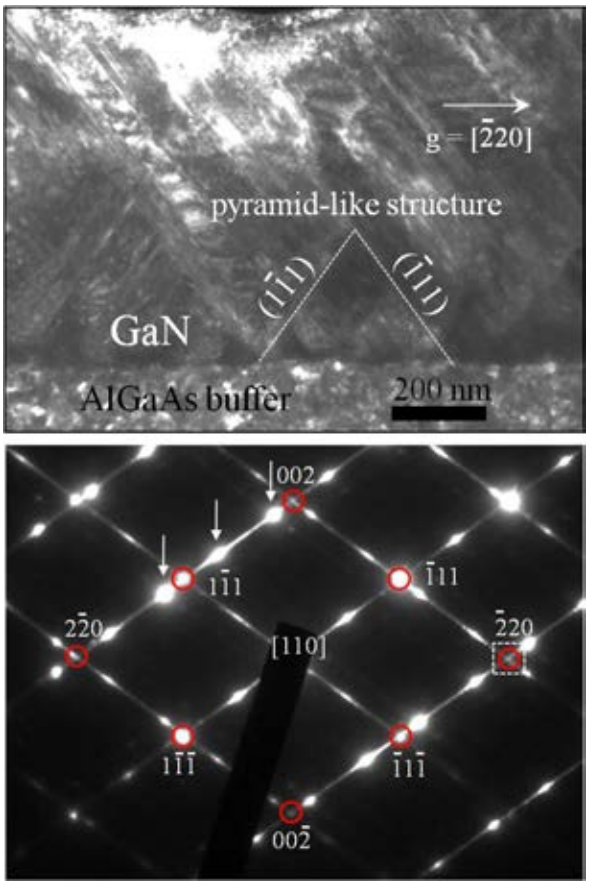

Figure 5.4: (a) Dark-field cross-sectional TEM image of c-GaN layer on GaAs (001) substrate with AlGaAs buffer layer taken along the [110] zone axis with diffraction from the ($\bar{2}$20) plane (white square). (b) SAD patterns refer to c-GaN (red circles) and h-GaN (white arrows) structures.

Cross-sectional TEM image taken along [1$\bar{1}$0] zone axis of other regions and selected area electron diffraction pattern as shown in Fig.5.5. BF TEM image of GaN layer showed different defect types, which are SFs and TDs are found in these [1$\bar{1}$0] direction. The tri-angle contrast is found at the interface generated from AlGaAs buffer layer around 400 nm above interface. The low density of SFs generated from the c-GaN/AlGaAs interface that decreases toward the sample surface. TDs are found over SFs that generated from the middle to the top layer of c-GaN, parallel to the [001] direction. The selected area diffraction (SAD) pattern obtained from the top of c-GaN where content the TDs showed single crystal of c-GaN. The TDs in GaN layer taken along [1$\bar{1}$0] zone axis are produced by a coalescence of pyramid-shaped grains in the [1$\bar{1}$0] direction [50].

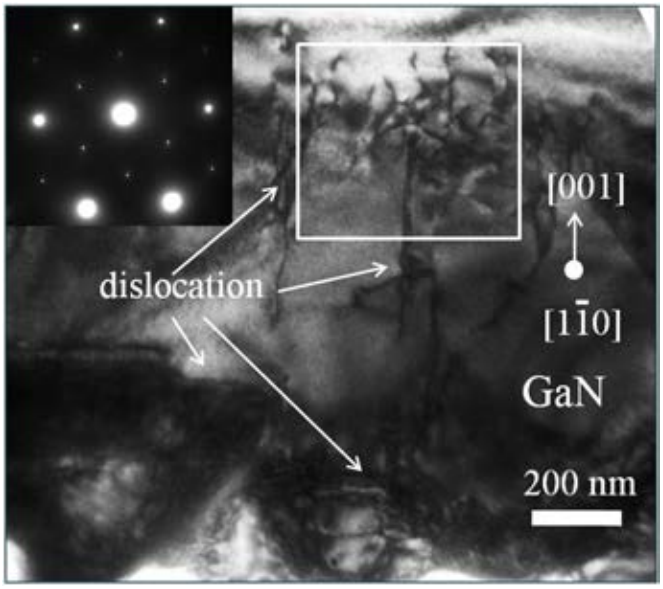

Figure 5.5: Cross-sectional TEM image of c-GaN layer grown on AlGaAs buffer layer/GaAs (001) substrate taken along [1$\bar{1}$0] zone axis at the c-GaN layer and their selected area electron diffraction pattern.

5.2.2 Evolution of phase structure in c-GaN

The evolution of phase structure in GaN layer taken along $[1\bar{1}0]$ zone axis as shown in Fig.5.6 that investigated by their corresponding SAD patterns. The BF cross-sectional TEM image of GaN film with AlGaAs buffer layer showed the tri-angle contrast at the GaN layer near interface. Above the tri-angle contrast are found the dislocation in GaN layer. The SAD pattern showed c-GaN/h-GaN mixed phase that taken from area near GaN/AlGaAs interface. But the SAD taken from middle and top layer area showed the single crystal of c-GaN. Although the area near interface are mixed phases between c-GaN and h-GaN, the area above tri-angle contrast mixed phases is wide area of single c-GaN structure. Therefore, the best quality of c-GaN with less hexagonal phase was achieved from this zone axis that caused the smooth surface and fairly flat of AlGaAs buffer surface in $[1\bar{1}0]$ zone axis. In addition, the c-GaN (111) and h-GaN (0002) diffraction spots are overlapped, so the epitaxial relationship between cubic and hexagonal GaN is $\{0001\}_{\text{h-GaN}}//\{111\}_{\text{c-GaN}}$ and $[11\bar{2}0]_{\text{h-GaN}}//[1\bar{1}0]_{\text{c-GaN}}$.

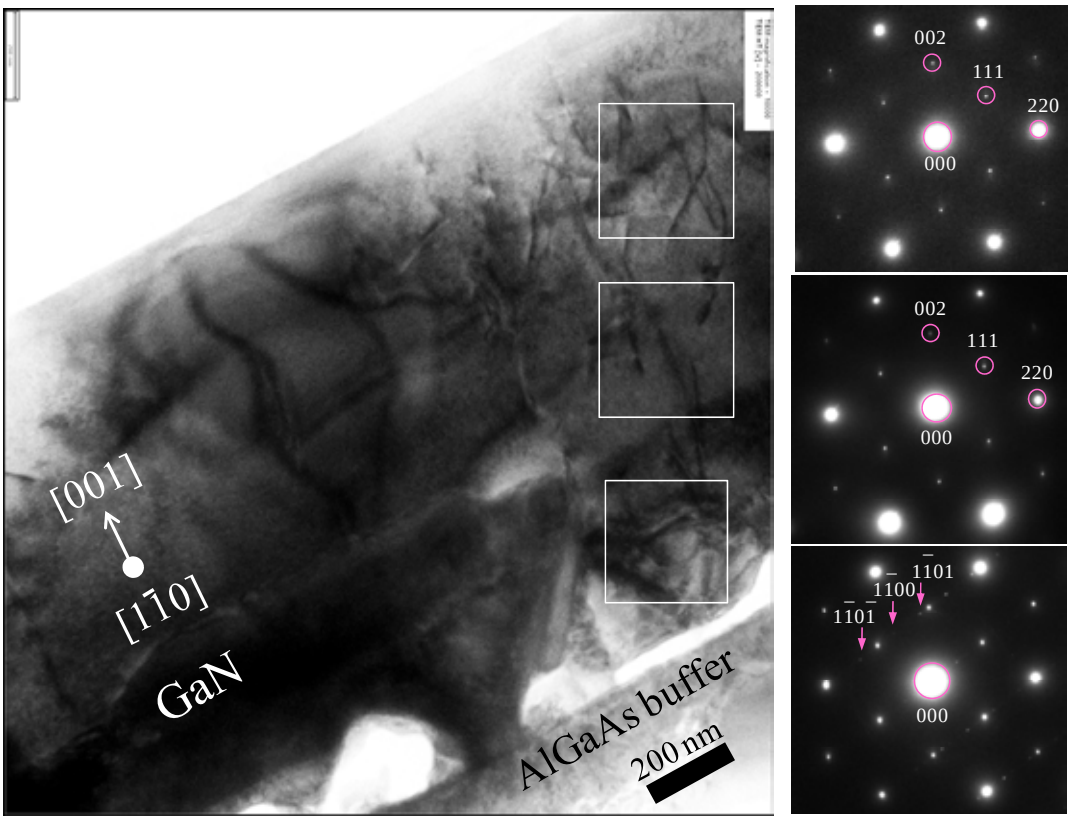

Figure 5.6: Cross-sectional TEM image of c-GaN layer grown on AlGaAs buffer layer/GaAs (001) substrate taken along [1$\bar{1}$0] zone axis and their corresponding selected area electron diffraction pattern showing evolution of phase structure in GaN layer.

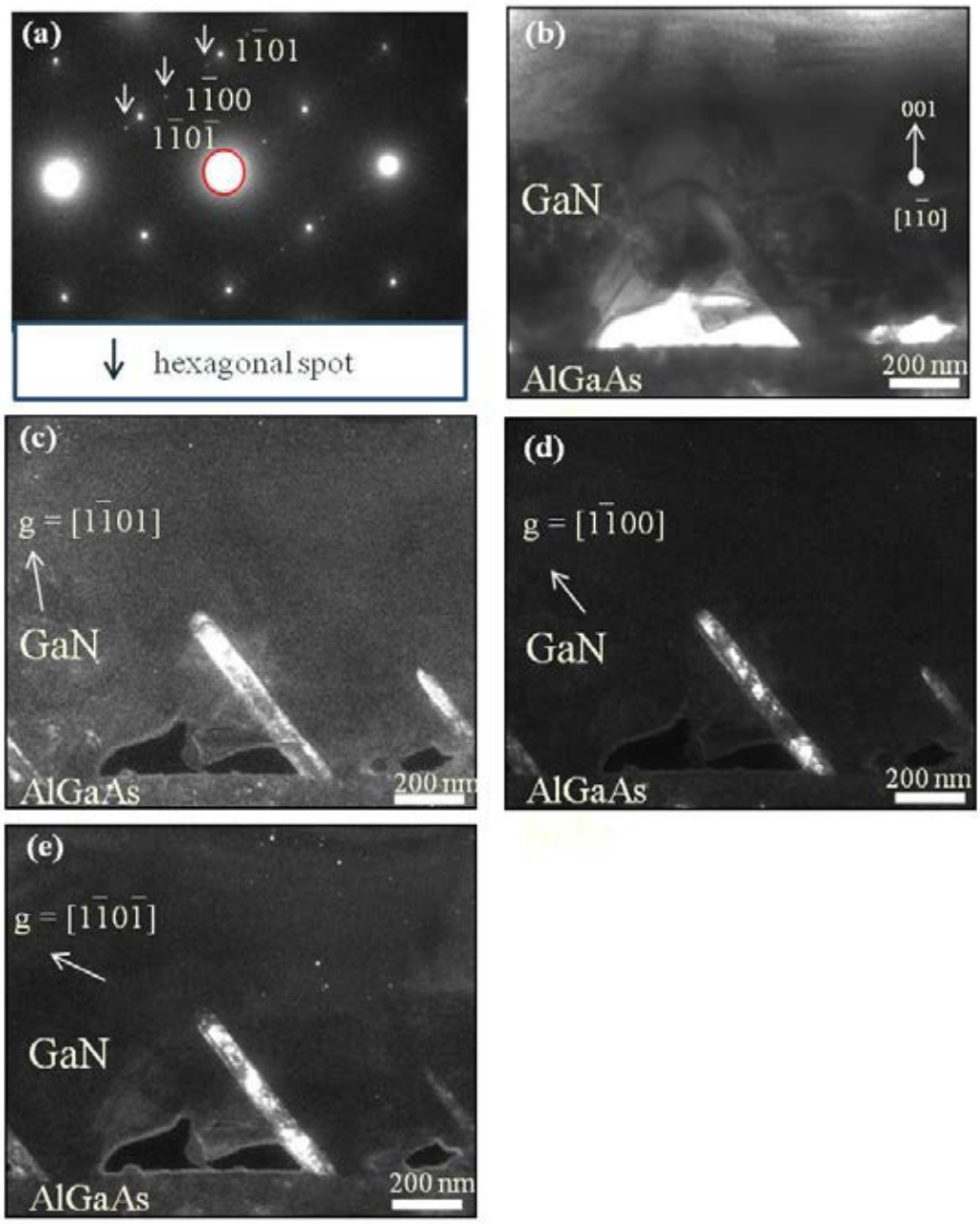

Figure 5.7: Cross-sectional TEM image of c-GaN layer grown on AlGaAs buffer layer/GaAs (001) substrate taken along [1$\bar{1}$0] zone axis showing (a) the SAD pattern of GaN layer, (b) bright field image of c-GaN at the interface region and (c-e) dark field images taken with reflections along g = [1$\bar{1}$01], g = [1$\bar{1}$00] and g = [1$\bar{1}$0$\bar{1}$], respectively.

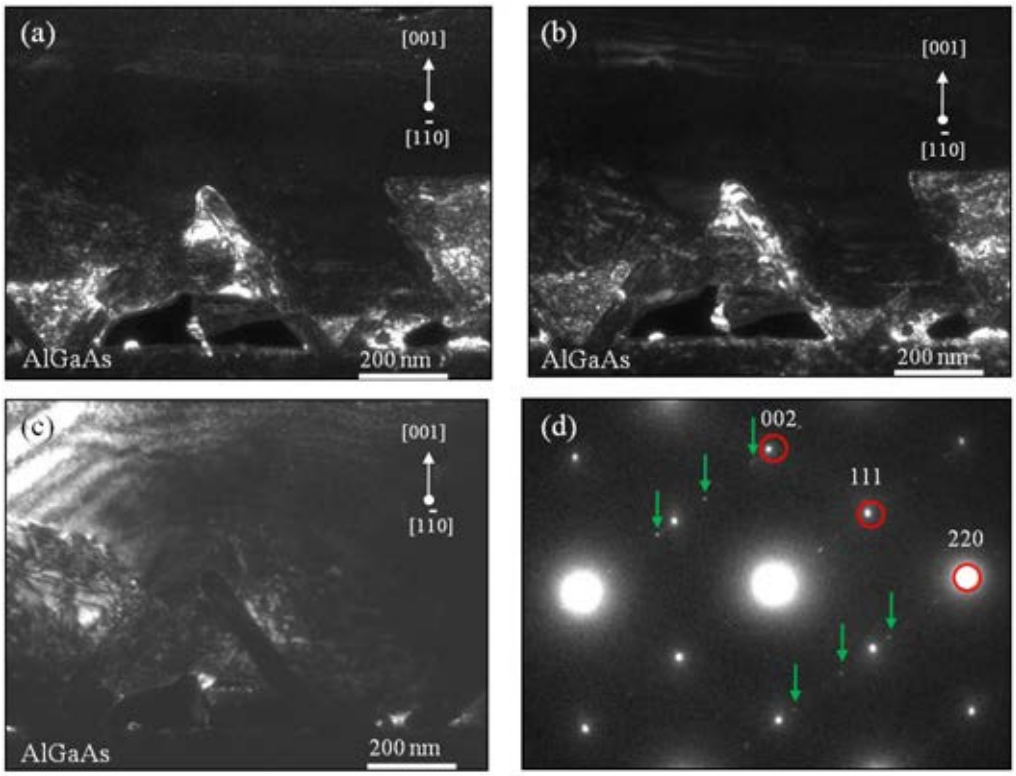

Figure 5.8: Cross-sectional TEM image of c-GaN layer at the interface region grown on AlGaAs buffer layer/GaAs (001) substrate taken along [1$\bar{1}$0] zone axis showing (a-c) dark field images taken with reflections along g = [002], g = [111] and g = [220], respectively and (d) the SAD pattern of GaN layer.

The evolution of phase structure at GaN layer near interface area found mixed phase of c-GaN and h-GaN. In order to investigate the hexagonal phase inclusion in c-GaN used the DF TEM images which diffracted from hexagonal phase. Figure 5.7(a) showed the SAD pattern and their corresponding bright field cross-sectional TEM image taken along [1$\bar{1}$0] zone axis that focused at interface of c-GaN layer showing the hexagonal phase contain in c-GaN as shown in Fig.5.7(b). The dark field cross-sectional TEM images obtained from the (1$\bar{1}$01), (1$\bar{1}$00) and

($1\bar{1}0\bar{1}$) diffraction spots show the regions corresponding to these hexagonal planes as shown in Fig.5.7(c)-5.7(e). The bright contrast regions within c-GaN layer correspond with hexagonal phase that proposed to construct form SFs and generated along the c-GaN {111} facets from interface of c-GaN/AlGaAs buffer. The bright contrast area showed hexagonal phase inclusion along (111) facet of c-GaN which is height around 400 nm from interface and width around 60 nm. Figure 5.8 showed the DF cross-sectional TEM image taken along [$1\bar{1}0$] zone axis. The dark field cross-sectional TEM images obtained from the (002), (111) and (220) diffraction spots show the regions corresponding to these cubic phase structure as shown in Fig 5.8(a)-5.8(c). The bright contrast regions represent the cubic phase in these regions which exist in tri-angle area near the interface mixing with SFs along (111) facet of c-GaN film. The SAD pattern showed the mixed phase between cubic phase structure and hexagonal phase structure (green arrow). It is clearly seen from cross-sectional TEM image taken along [$1\bar{1}0$] zone axis showed the less SFs to compare with the density of SFs taken along [110] zone axis showing pyramid-like structure.

5.2.3 Investigation of structural defects

The BF cross-sectional TEM image taken along [$1\bar{1}0$] zone axis of GaN film with AlGaAs buffer layer as shown in Fig. 5.9(b) which is not clearly seen the defect and the growth formation in c-GaN. The SAD pattern in Fig.5.9(a) taken from GaN layer showed cubic phase pattern without streaking. But 6 diffraction spots from plane ($\bar{2}\bar{2}0$), (220), ($\bar{1}\bar{1}3$), (113), ($\bar{1}\bar{1}\bar{3}$) and ($11\bar{3}$) have higher intensity that expected due to emerged with diffraction spots from another zone axis. The dark field image

from Fig.5.9(d) and Fig.5.9(f) showed the bright contrast from area near interface that found the tri-angle shaped contrasts due to a coalescence of pyramid shaped grains in the [1$\bar{1}$0] direction. For the 6 intent spots, are expected due to emerged with diffraction spots from twin boundary along [$\bar{1}$14$\bar{4}$] zone axis [51]. These reflection plane from [$\bar{1}$14$\bar{4}$] zone axis are ($\bar{2}\bar{2}$0), (220), (1$\bar{3}$1), (3$\bar{1}$1), ($\bar{3}$1$\bar{1}$) and ($\bar{1}$3$\bar{1}$) respectively (green circle) as shown in Fig.5.10(a). The twin boundary in [$\bar{1}$14$\bar{4}$] zone axis generated by insert 1 mono layer of h-GaN along (111) of c-GaN.

For the dark field image taken from plane ($\bar{1}\bar{1}$3) and ($\bar{2}\bar{2}$0) showed the bright contrast at top area of GaN film as shown in Fig.5.9(c) and Fig.5.9 (e) that showed the dislocations in the line contrast over the tri-angle shaped contrast. For the DF TEM images taken from the ($\bar{1}\bar{1}$3) and (11$\bar{3}$) reflection pairs showed the 2 bright contrast boundary at the top area and bottom area, respectively as shown in Fig.5.9(c) and Fig.5.9(d). Whereas, the ($\bar{2}\bar{2}$0) and (220) reflection pairs showed the bright contrast area in two boundary as shown in Fig.5.9(e) and Fig.5.9(f). The two different boundary known as the antiphase boundary (APB) that are expected to see in the {001}, {011}, {111}, {112} and {113} planes for III-V compound [52]. For the APB at the III-V nitride such as GaP occurred by mono-atomic steps at the Si and Ge surface substrate [53, 54, 55]. The model of two boundaries between top area and tri-angle shaped area formed by the wrong bond of Ga-Ga and N-N at the interface of APB showing (111) to bound the (001) plane of c-GaN (yellow area) as shown in Fig.5.10(b). Figure 5.10(c) show the model of twin boundary along [$\bar{1}$14$\bar{4}$] zone axis and APB of this twin boundary leading to the two boundaries between top and bottom area.

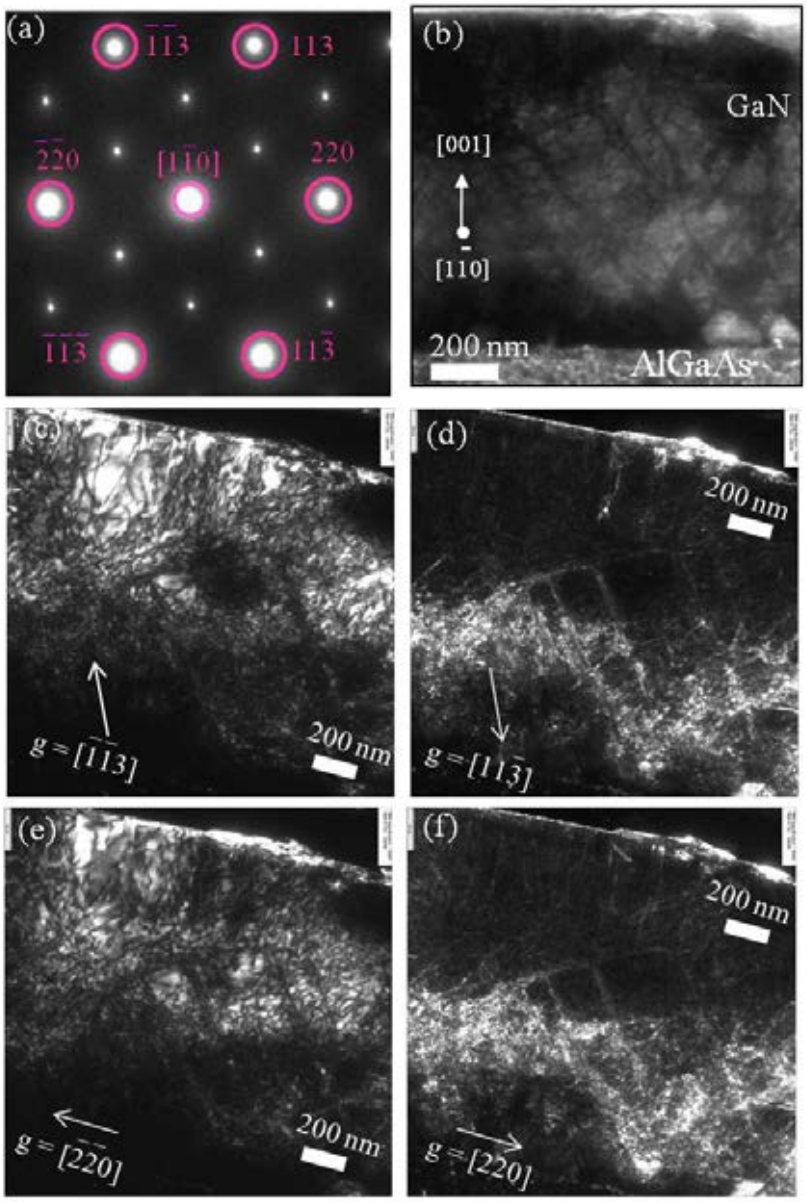

Figure 5.9: (a) SAD pattern of (b) BF image of c-GaN film grown on AlGaAs/GaAs (001) substrate, the cross-sectional dark field TEM images obtained from diffraction spots ($\bar{1}\bar{1}3$), ($11\bar{3}$), ($\bar{2}\bar{2}0$) and (220) plane as showed in (c), (d), (e) and (f) respectively.

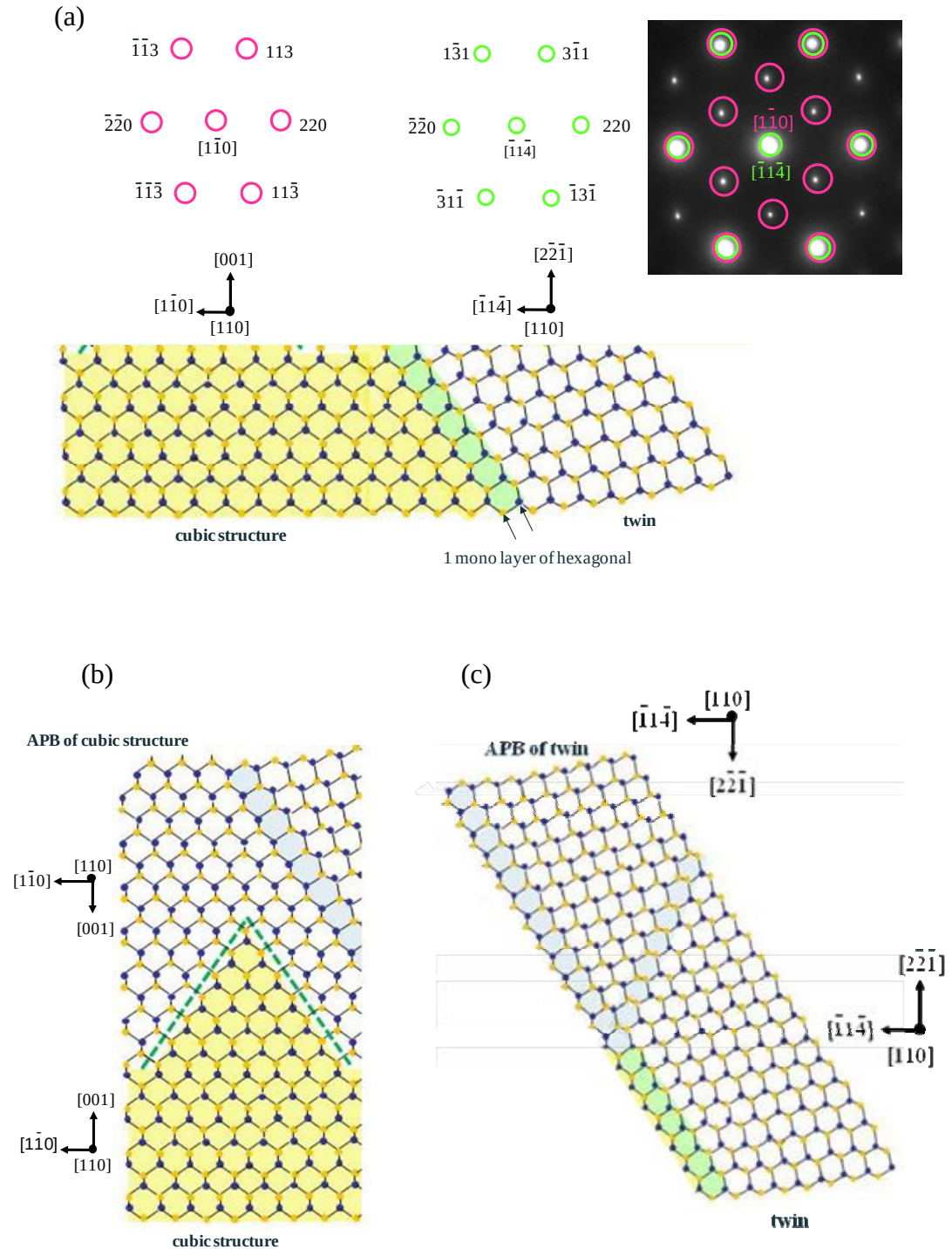

Figure: 5.10 Schematic illustration of defect distribution in c-GaN show (a) twin boundary $[\bar{1}1\bar{4}]$, (b) APB between top and bottom region and (c) twin and APB of twin region.

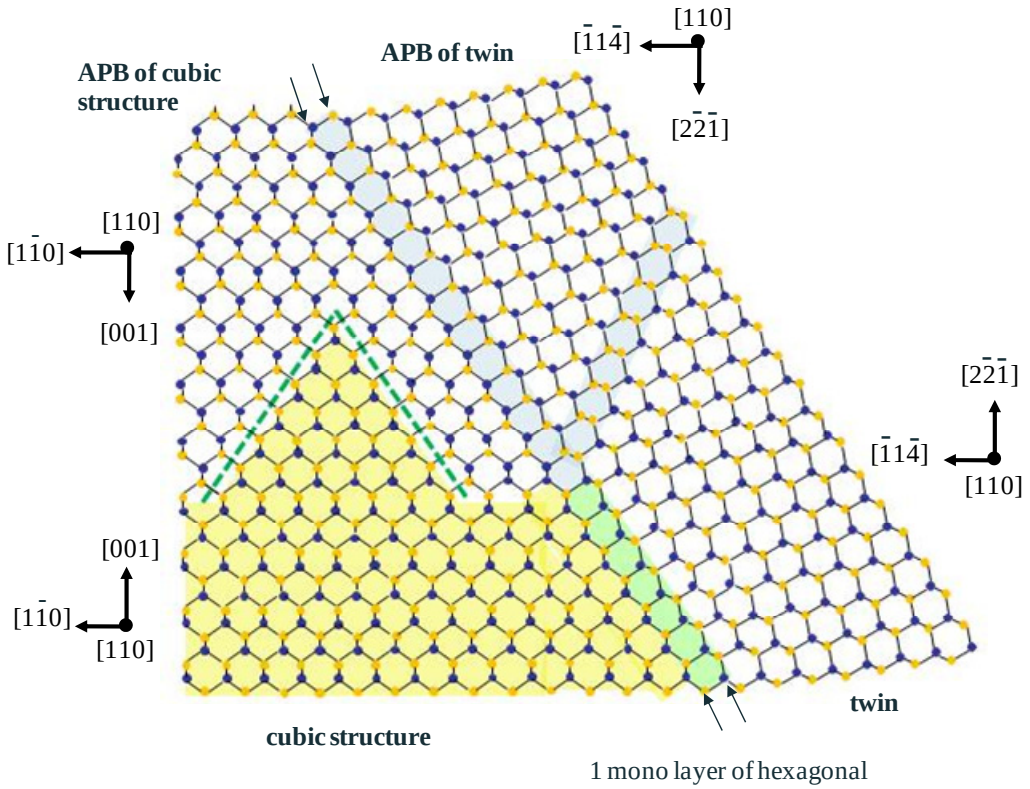

Figure 5.11: Schematic illustration of two-dimensional lattice of c-GaN revealing the APB and twin boundary along the [$1\bar{1}0$] zone axis.

A model of defect distribution in c-GaN with APB and twin boundary taken along [$1\bar{1}0$] and [$\bar{1}1\bar{4}$] zone axis to explain DF TEM images in the whole layer as shown in Fig.5.10. The ED pattern have both of small and big spot around the direct spot (000) that used for creating dark field image to observe the growth mechanism. The dark field image taken from (002), (111) and ($11\bar{1}$) planes that demonstrated the small bright contrast area and almost dark area of GaN film layer showing in Fig.5.12(b)-

Fig.5.12(d), respectively. Therefore, dark field from small spot cannot clearly observe the growth mechanism of GaN film layer.

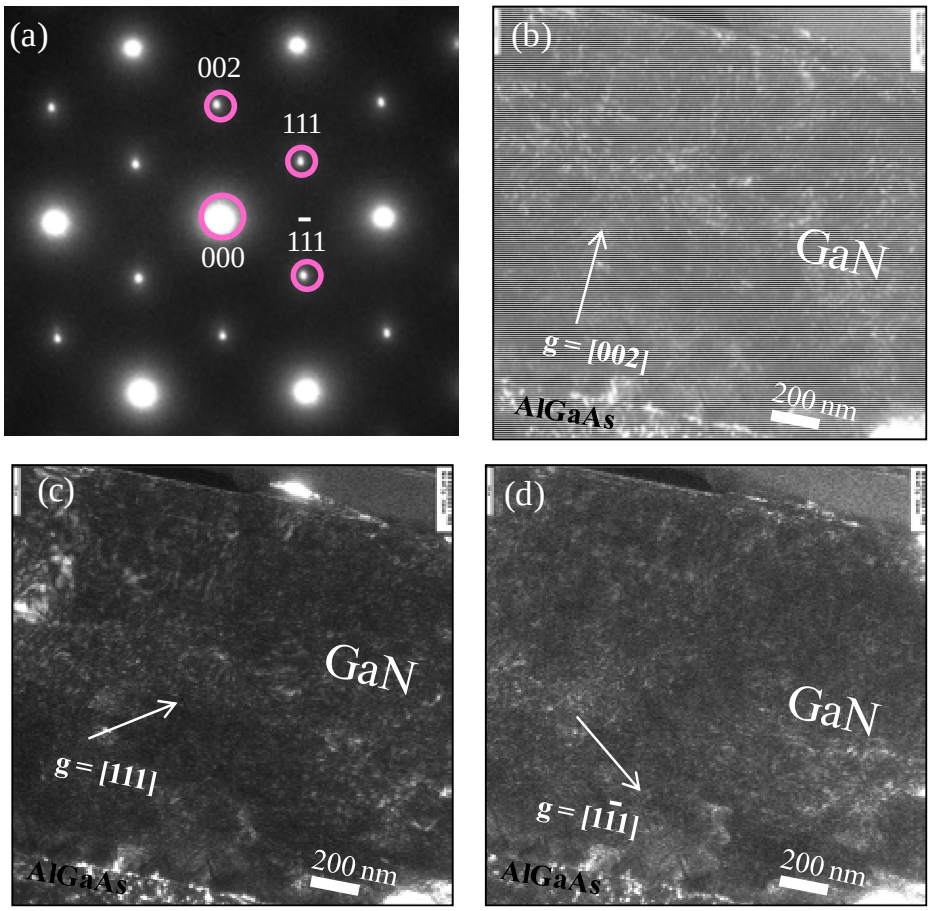

Figure 5.12: (a) SAD pattern of c-GaN film grown on AlGaAs/GaAs (001) substrate taken along [1$\bar{1}$0] zone axis, (b) cross-sectional dark field TEM images obtained from diffraction spots (002), (c) (111) and (d) (11$\bar{1}$) planes.

5.3 Summary

The effects of the AlGaAs buffer layer inserted between GaN film and GaAs (001) substrate, that was successfully to protect the GaAs surface from thermal decomposition, were investigated by TEM. It is clearly seen that no voids were observed at the c-GaN/AlGaAs buffer layer both of [110] and [1$\bar{1}$0] zone axis. Moreover, TEM analysis found the AlGaAs buffer layer can induces the anisotropic defect which are SFs and TDs distribution. This anisotropic of SFs distribution is likely to be associated with the different atomic structure of surface step along [110] and [1$\bar{1}$0] crystallographic direction on the (001) AlGaAs. High density of SFs are found in [110] direction that associated with atomic (111) steps at the c-GaN/AlGaAs interface lead to formation seed of SFs. The DF TEM images taken along [1$\bar{1}$0] zone axis reveal the twin boundary along [$\bar{1}$1$\bar{4}$] zone axis and APB in c-GaN layer. However, the growth condition of AlGaAs buffer layer will improve to decrease the surface roughness showing (111) step which is an origin of SFs and hexagonal phase.

CHAPTER VI

ANALYSIS OF STRUCTURAL PHASE TRANSITION IN c-InN INDUCED BY THE HEXAGONAL PHASE CONTAINED IN c-GaN NUCLEATION LAYER

6.1 Growth conditions and sample's details

Cubic-InN films were grown on MgO (001) substrate with c-GaN buffer layer by RF-N_2 plasma MBE (Molecular Beam Epitaxy). The 400 nm thickness of c-GaN buffer layer as a nucleation layer of c-InN film, were grown on (001) MgO substrate at 700°C. The c-InN films were grown for 1 hour at 475°C-500°C with various III/V ratios (In flux) as shown the growth condition in Fig.6.1.

According to S. Kuntarin [56] estimated the hexagonal phase content in both of c-InN film and c-GaN buffer layer, by using high resolution X-ray diffraction (HRXRD) from the ratio of the integrated x-ray diffraction intensities of the cubic (002) and hexagonal ($10\bar{1}1$) planes measured by ω-scan in the x-ray reciprocal space mapping (RSM). The content of hexagonal phase inclusion in c-InN films and c-GaN buffer layer showed in Table 6.1. The assumption from data in Table 6.1, the hexagonal phase content in c-GaN layer increase leading to higher of hexagonal phase content in c-InN layer.

In this work, the crystal structure and the mechanism of h-InN generated in c-InN films propagating from GaN buffer layer were investigated by TEM. To study the growth condition is affecting on the quality of c-InN and leading to mix with different hexagonal content in c-InN layer. Changes of the growth condition affecting on the surface morphology was investigated by AFM.

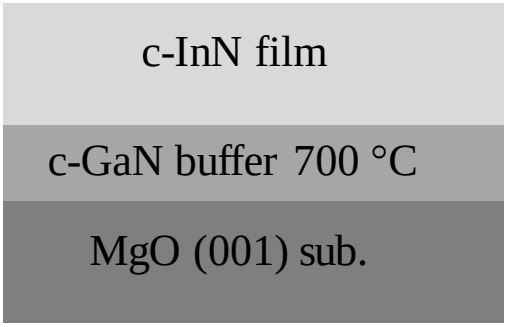

Figure 6.1: The growth condition of c-InN films grown on MgO (001) substrate using c-GaN buffer: growth temperature of c-InN layer sample (a) 500°C with In flux: 8×10^{-5}Pa, sample (b) 475°C with In flux: 8×10^{-5}Pa and sample (c) 475°C with In flux: 4×10^{-5}Pa.

sample	Hexagonal phase inclusion (%)	
	c-GaN buffer layer	c-InN film
A	2	8
B	4	15
C	8	24

Table 6.1**:** Amount of hexagonal phase inclusion in c-InN films and c-GaN buffer layer.

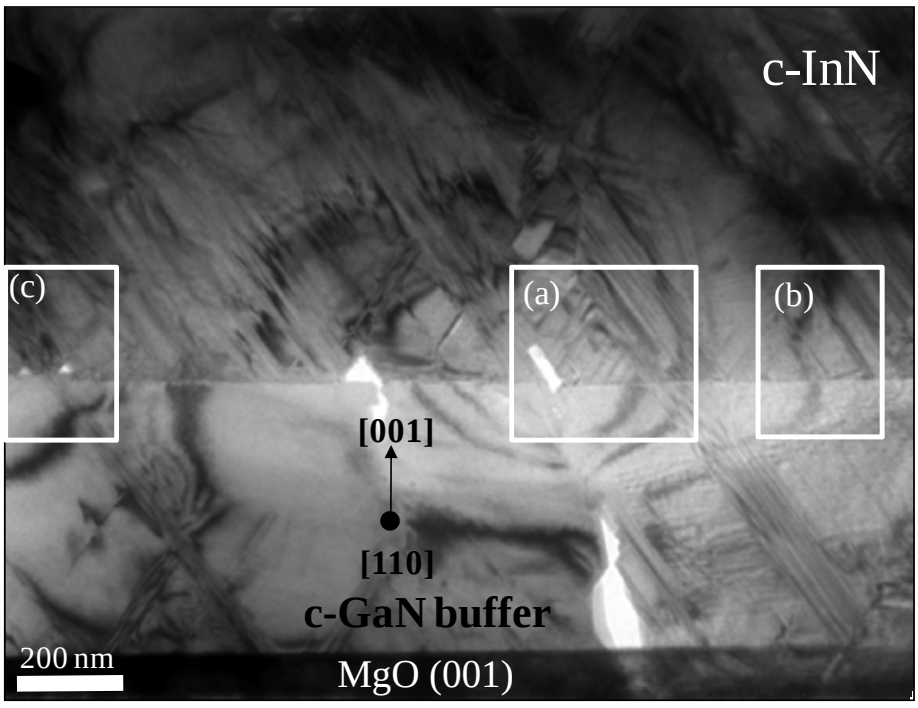

Figure 6.2: Cross-section BF TEM image of c-InN (92%) / c-GaN (98%) buffer on (001) MgO substrate.

6.2 Effect of h-GaN buffer (2%) on h-InN in c-InN layer

A high cubic phase purity of 92% for the c-InN with 8% of hexagonal phase inclusion grown on cubic phase purity of 98% for c-GaN buffer layer with 2% of hexagonal phase inclusion was investigated the crystal structure and defect structure as shown in Fig.6.2. The BF cross-sectional TEM image taken along [110] zone axis showed the 3 layers of c-InN film/c-GaN buffer layer on MgO (001) substrate. In the c-GaN buffer layer found a few of planar defects generated from interface of c-GaN buffer/MgO (001) substrate that along the (111) facet of c-GaN buffer layer penetrate to the c-InN film. These SFs interact with another one and stop their propagation. But some parts of SFs extend to the InN layer by decreasing when away from the interface. The focus interface of planar defect as SFs from interface of c-GaN buffer layer propagated to the c-InN films as shown in Fig.6.3 taken from area (a) of Fig.6.2. The c-InN film layer are found the pyramid like structure showing (111) facet that proposed as planar defect such as SFs and twin. These planar defects generated from the interface of c-InN/c-GaN buffer without and with the planar defect propagated continually from c-GaN buffer layer. The density of planar defect generated on c-InN film is higher than c-GaN buffer layer corresponding with calculate the amount of hexagonal phase in c-GaN buffer and c-InN layer. The BF cross-section TEM image taken from area (b) of Fig.6.2 showed the interface of c-InN and c-GaN buffer is generally smooth. The less planar defect are found both of c-InN film and c-GaN buffer layer that focus at interface as shown in Fig.6.4. The SAD pattern taken from the interface area of c-InN and c-GaN layer showed the cubic phase pattern of c-InN and c-GaN buffer with streaking due to SFs. The BF cross-sectional TEM image taken from area (c) of Fig.6.2 demonstrated a few SFs that propagated from c-GaN

buffer layer to the c-InN film as shown in Fig.6.5(a). But there is high density of SFs in c-InN film generated from interface between c-InN and c-GaN buffer layer despite without the SFs propagated from c-GaN buffer layer. In Fig.6.5(c), the SAD pattern of c-InN and c-GaN buffer layer which demonstrate 2 ED pattern of c-InN film (inner pattern) and c-GaN buffer layer (outer pattern), showed the cubic phase pattern with streaking due to planar defect. There is a small incorporation of hexagonal phase in SAD pattern that proposed in form of planar defect such as SFs due to high density of SFs can become seed of h-GaN. Dark field (DF) image taken from $(\bar{1}11)$ plane of c-InN was found the bright contrast of cubic phase plane $(\bar{1}11)$ along the (111) facet of c-InN as shown in Fig6.5(b).

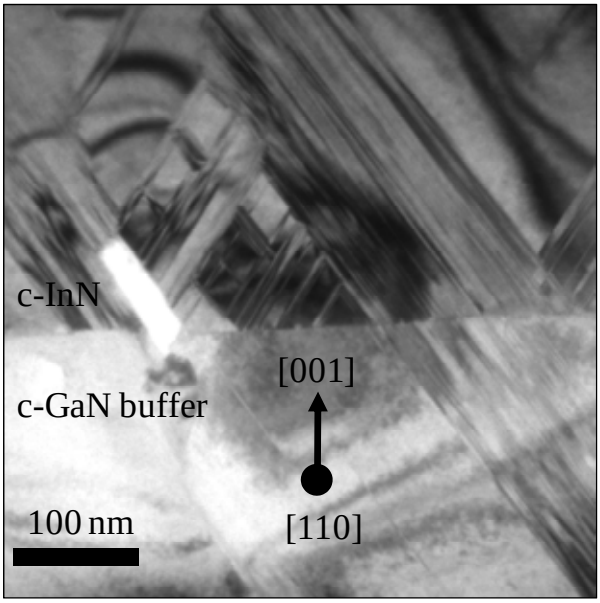

Figure 6.3: The BF cross-sectional TEM image taken along [110] zone axis showed SFs propagated from c-GaN buffer to c-InN film.

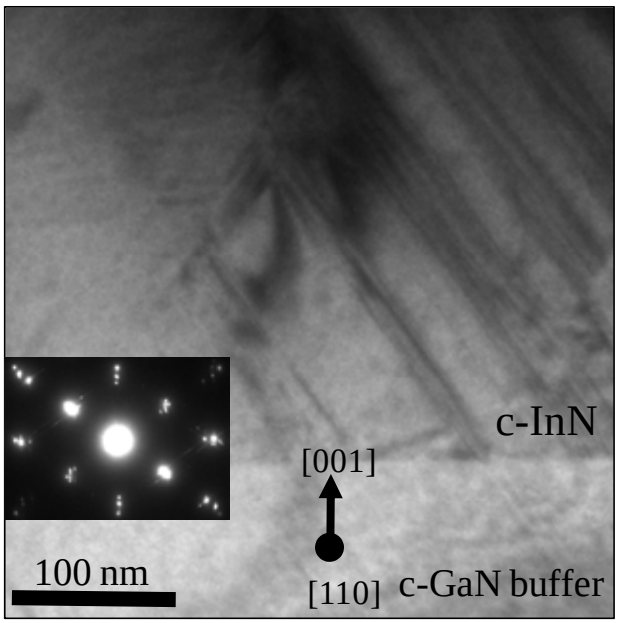

Figure 6.4: the BF cross-sectional TEM image taken along [110] zone axis showed less SFs between interface and the SAD of c-InN film/c-GaN buffer.

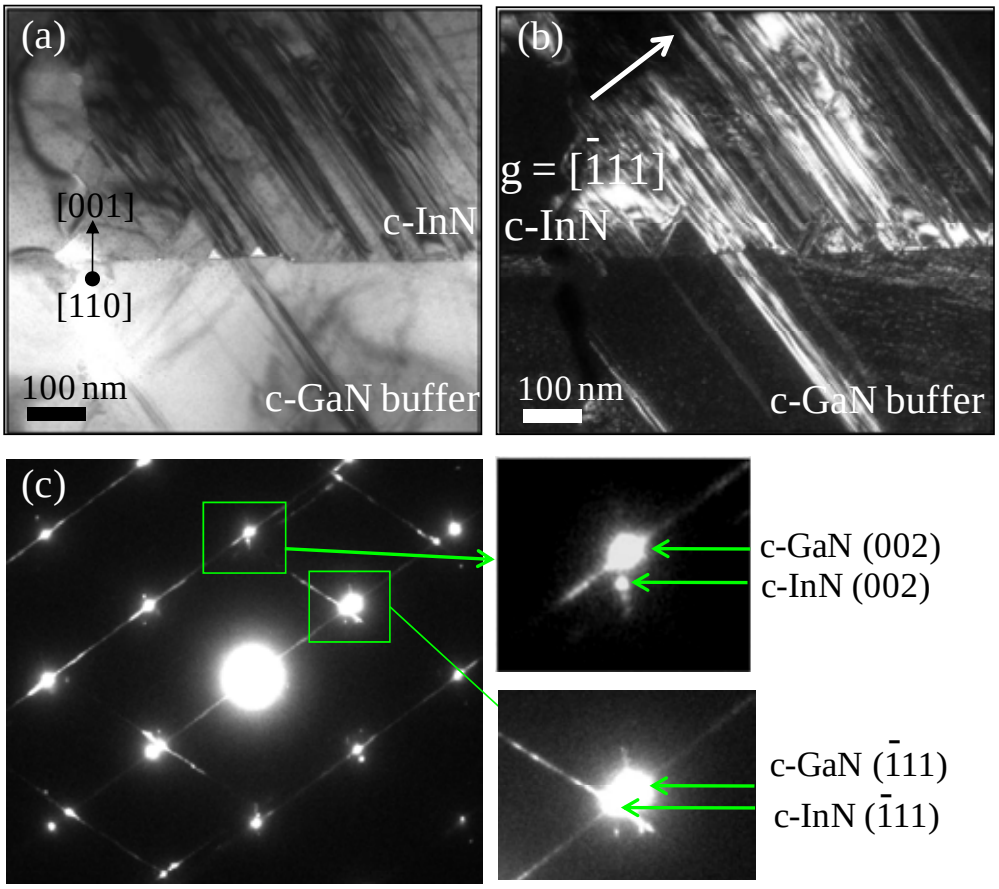

Figure 6.5: cross-sectional TEM image of c-InN with 8% of hexagonal phase inclusion and c-GaN buffer layer with 2% of hexagonal phase inclusion showed (a) BF image, (b) DF image and (c) the SAD pattern of c-InN and c-GaN buffer with streaking.

6.3 Effect of h-GaN buffer (4%) on h-InN in c-InN layer

TEM was used to investigate the hexagonal phase formation in c-InN film with 15% hexagonal phase inclusion and c-GaN buffer layer with 4% of hexagonal phase inclusion. The BF cross-sectional TEM image of cubic phase purity of 85% for c-InN film and cubic phase purity of 96% for c-GaN buffer layer taken along [110] zone axis were shown in Fig.6.6(b). The SAD pattern of c-InN film (blue circle) and c-GaN buffer layer (pink circle) shows a combination between cubic phase and hexagonal phase. Apparently, the hexagonal spots (green arrow) from c-InN film are more than hexagonal spots from c-GaN buffer due to the higher amount of h-InN as shown in Fig.6.6(a). The DF cross sectional TEM images taken from $(1\bar{1}00)$ and $(1\bar{1}01)$ plane of h-InN are shown in Fig.6.6(c) and Fig. 6.6(d). The bright contrast represent hexagonal phase inclusion of c-InN proposed in a form of planar defect such as SFs and twin along the (111) facet. These planar defects propagated from an interface between c-GaN buffer and c-InN layer to the whole layer of c-InN film.

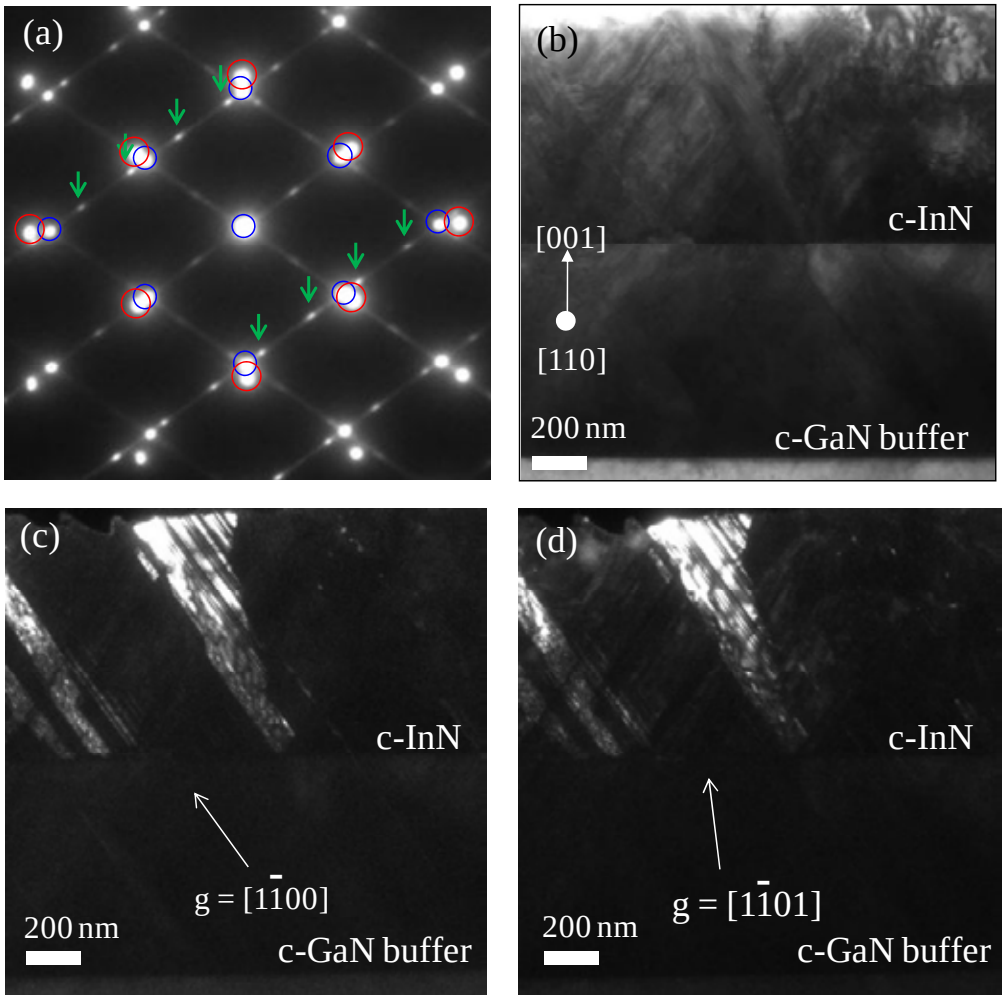

Figure 6.6: Cross-sectional TEM image of c-InN with 15% of hexagonal phase inclusion showed (a) the SAD pattern of c-InN and c-GaN buffer, (b) BF image, and (c)-(d) the DF image taken from $(1\bar{1}00)$ and $(1\bar{1}01)$ plane, respectively.

To investigate the hexagonal phase in c-GaN buffer layer propagate to the hexagonal phase in c-InN films, reflection plane ($1\bar{1}0\bar{2}$) was taken from both of InN film and GaN buffer as shown in Fig.6.7(a). The bright contrast line along (111) facet of c-GaN buffer layer are not continue to the bright contrast area along (111) facet of c-InN film as shown in Fig.6.7(b). These result indicate the hexagonal phase in c-GaN buffer not propagating to the hexagonal phase in c-InN film which generated from interface between c-InN/c-GaN. The DF cross-sectional TEM image taken along [110] zone axis which were taken with reflection from cubic phase along (c) hkl = $1\bar{1}1$ and (d) hkl = $\bar{1}11$ both of c-InN film and c-GaN buffer as shown in Fig. 6.7(c) and Fig. 6.7(d). The dark contrast regions within the c-InN layer and c-GaN buffer correspond to the hexagonal phase inclusion and planar defect such as SFs and twins which showing ($1\bar{1}1$) and ($\bar{1}11$) which is look like penetrate into the whole layer of c-InN film. The less planar defect in c-GaN buffer layer propagated to the c-InN layer.

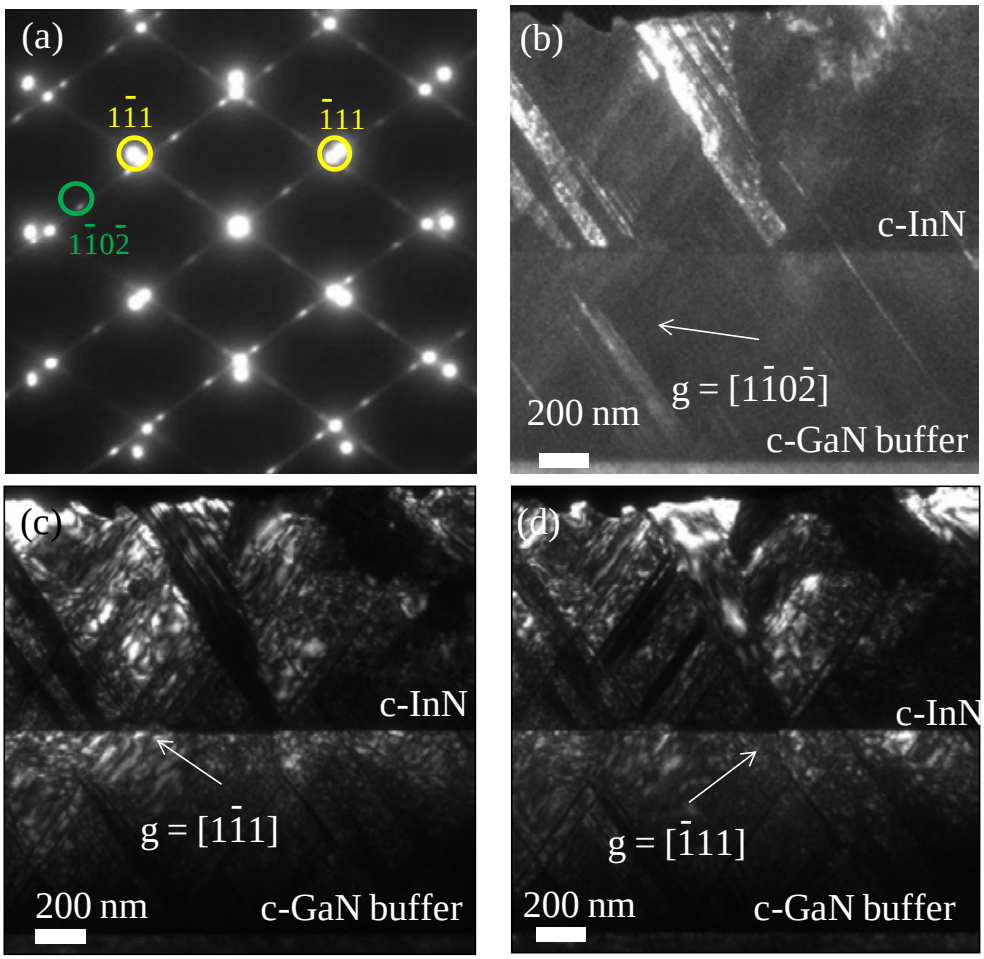

Figure 6.7: Cross-sectional TEM image of c-InN with 15% of hexagonal phase inclusion showed (a) the SAD pattern of c-InN and c-GaN buffer taken from (b) $(1\bar{1}0\bar{2})$, (c) $(1\bar{1}1)$ and (d) $(\bar{1}11)$, respectively.

6.3.1 Occurrence of forbidden diffraction

The SAD patterns of c-InN film/c-GaN buffer in [110] zone axis with the SAD pattern of hexagonal phase in [11$\bar{2}$0] zone axis are shown in Fig. 6.8(a). The diffraction spot of allowed reflection plane in hexagonal phase (green arrow) mixed with the forbidden plane as {0001} (red circle). The DF TEM images taken from forbidden plane (0001) and (000$\bar{1}$), show the bright contrast area of hexagonal phase. Therefore, these forbidden reflection planes are expected from double diffraction of hexagonal phase structure as shown in Fig. 6.8(b) and Fig.6.8(c). The double diffraction to form (0001) plane of hexagonal phase can be illustrated by Fig.6.8(d). The diffraction spot from (1$\bar{1}$00) and (1$\bar{1}$01) have g_1 and g_2, respectively. If the first diffraction plane (1$\bar{1}$00) leads to diffraction spot at (1$\bar{1}$00) and acts as an incident beam to re-diffract by the (1$\bar{1}$01) plane. Therefore, the forbidden reflection plane at (0001) is generated by g_1+g_2 = [1$\bar{1}$00] + [1$\bar{1}$01] = [0001].

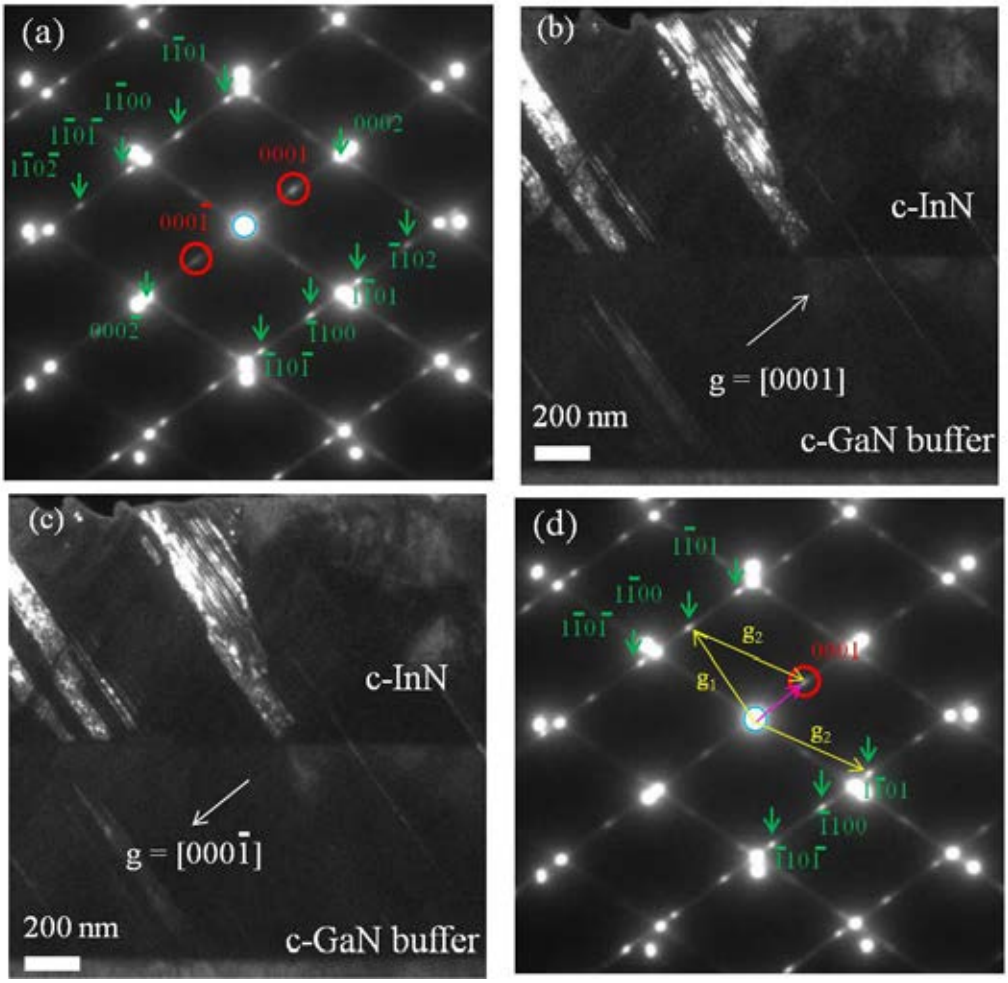

Figure 6.8: Cross-sectional TEM image of c-InN with 15% of hexagonal phase inclusion showed (a) the SAD pattern of hexagonal phase of c-InN taken along [11$\bar{2}$0], DF TEM image from reflection plane (b) (0001), (c) (000$\bar{1}$) and (d) double diffraction of (0001) plane.

6.4 Effect of h-GaN buffer (8%) on h-InN in c-InN layer

The cubic phase purity of 76% for c-InN film layer and cubic phase purity of 92% for c-GaN buffer was investigated by TEM. The BF cross-sectional TEM image of c-InN film with 24% of hexagonal phase inclusion grown on c-GaN buffer layer with 8% of hexagonal phase inclusion showed 3 layer of c-InN film and c-GaN buffer layer on MgO substrate which demonstrated the planar defect propagating from c-GaN buffer to c-InN film along the (111) facet of c-InN as shown in Fig.6.9(a). The planar defect in c-GaN buffer layer was generated from interface between c-GaN and MgO substrate. The SAD pattern both of c-InN film and c-GaN buffer showed the mixed between cubic phase and hexagonal phase of InN and GaN as shown in Fig.6.9(c). The hexagonal phase pattern in c-InN and c-GaN are clearly seen that marked with red arrow as shown in Fig.6.9(c). The dark field cross-sectional TEM image taken from $(\bar{1}100)$ plane both of h-InN and h-GaN as shown in Fig.6.9(b). The bright contrasts represent the hexagonal phase inclusion in c-InN and c-GaN that constructed in a form of planar defect along (111) facet of c-InN and propagated from c-GaN buffer to c-InN film. The amount of h-InN buffer layer is less than in h-InN film layer which expand in their lateral.

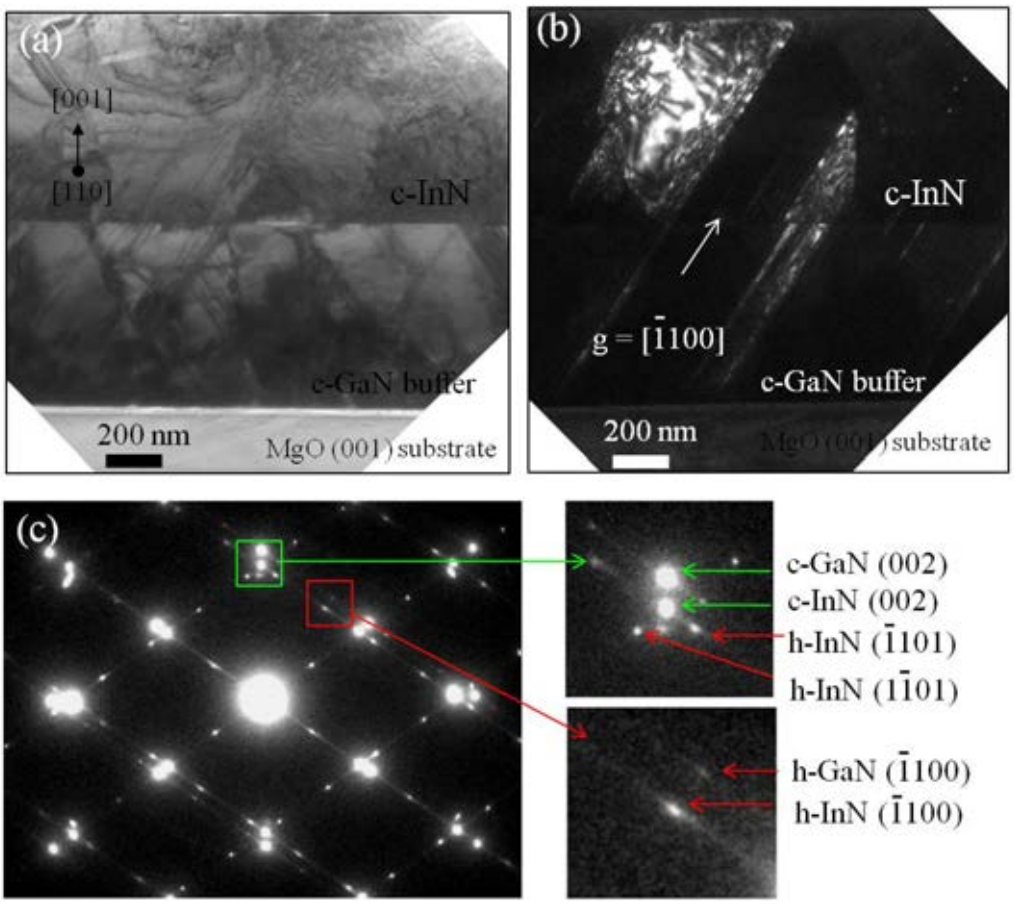

Figure 6.9: Cross-sectional TEM image of c-InN with 24% of hexagonal phase inclusion showed (a) BF image, (b) DF image and (c) the SAD pattern of c-InN and c-GaN buffer.

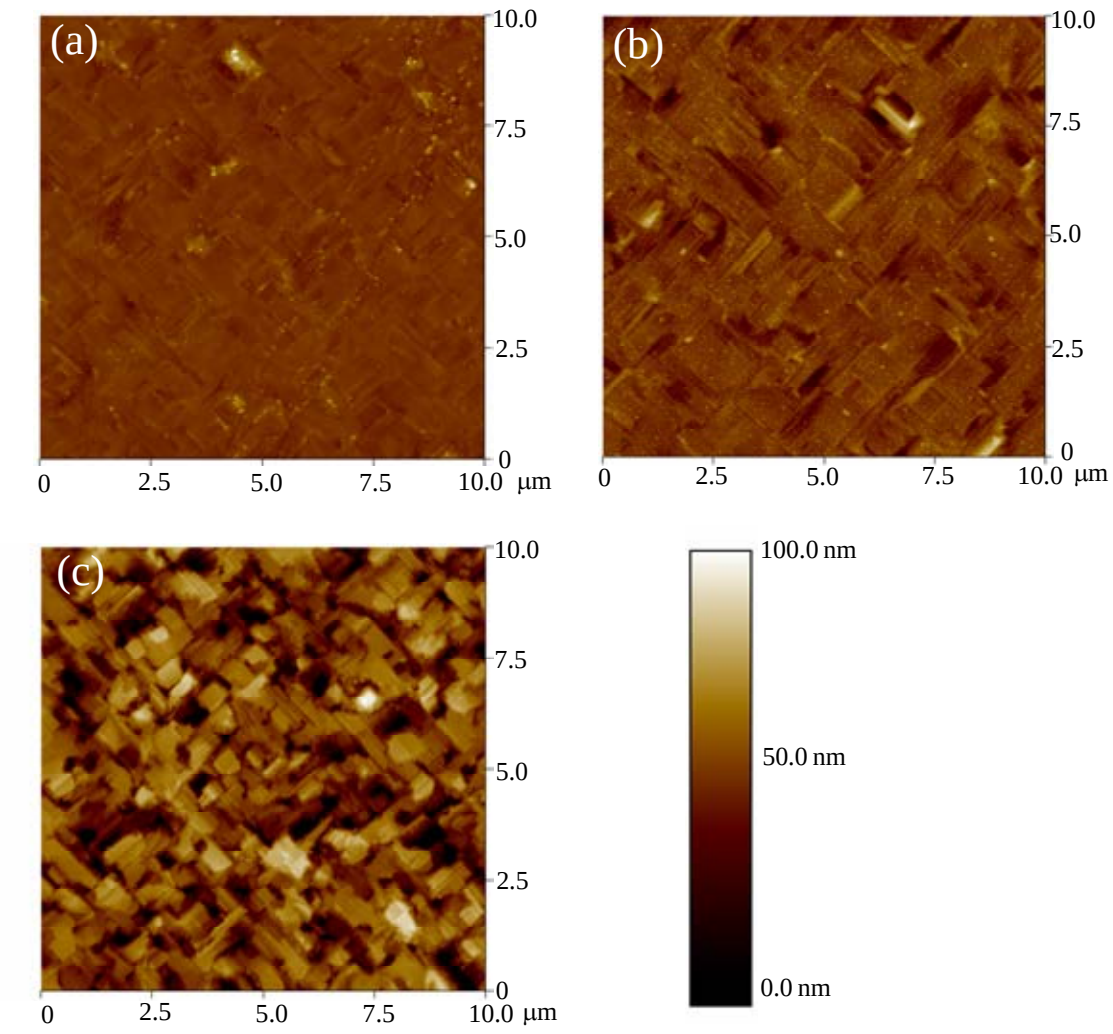

Figure 6.10: Surface morphology of c-InN grown on MgO (001) substrate using c-GaN buffer layer (a) sample A (growth at 500°C with In flux: $8x10^{-5}$ Pa), (b) sample B (growth at 475°C with In flux: $8x10^{-5}$ Pa) and (c) sample C (growth at 475°C with In flux: $4x10^{-5}$ Pa).

6.5 Surface morphologies of c-InN films

The surface morphology of c-InN grown on MgO (001) substrate using c-GaN buffer layer with different growth conditions were investigated by AFM. The formation of square grains at surface is attributed to the cubic InN (100) [57]. The surface of sample A grown at 500°C with In flux: $8x10^{-5}$ Pa is found the continually of square grains lead to the smooth surface as shown in Fig.6.10(a). In case of sample B, c-InN film grown at 475°C with In flux: $8x10^{-5}$ Pa showed the square grains with continue less than sample A as shown in Fig.6.10(b). The sample C, c-InN film grown at 475°C with In flux: $4x10^{-5}$ Pa showed the isolated square grains lead to high roughness of surface. The sample A is less hexagonal phase inclusions (8% of h-InN) in c-InN film. Therefore, c-InN grown at relative high temperature can improve both of flatness of surface and crystal quality of c-InN film. The c-InN film growth at relative high temperature is found to improve the flatness of films due to the controlled migration length of adatoms [44].

6.6 Summary

According to Y. Iwahashi [44], the growth condition effect on the quality of c-InN due to hexagonal phase inclusion decreased with an increasing of growth temperature and In flux. Cubic InN grown at relative high temperature can improve the flatness of surface and crystal quality of c-InN film. In case of a high cubic phase purity of 92% for c-InN film was grown at 500°C and In flux is 8×10^{-5} Pa that found the smooth surface and decreasing of the hexagonal phase content in c-InN. TEM is

used to investigate the formation of hexagonal phase inclusion (h-InN) in c-InN. The hexagonal phase inclusion in c-InN films constructed in a form of planar defect that was generated from an interface between c-GaN buffer layer and c-InN film which is not propagated from planar defect in c-GaN buffer layer to the c-InN layer.

CHAPTER VII

CONCLUSIONS

Effects of the buffer layer on the crystal quality and structural phase transformation in c-GaN and c-InN thin films grown on the (001) oriented substrates were systematically investigated by transmission electron microscopy (TEM). Analytical TEM techniques were used to analyze the formation of structural defects and their distribution. These results may be useful for an improvement of the growth conditions for higher purity c-GaN and c-InN films. The details are summarized as following.

(i) Crystal structure and quality of c-GaN films grown on GaAs (001) substrates by metalorganic vapor phase epitaxy (MOVPE) were verified to be affected by an insertion of the AlGaAs buffer layer. Our results clearly show that the AlGaAs inserted layer can protect a (001) GaAs substrate surface without any voids, which are generated due to thermal decomposition at high growth temperature (960^{o}C), leading to a smooth interface between c-GaN and AlGaAs buffer layer. Cross-section TEM images taken along the [110] zone axis reveal that the AlGaAs buffer layer induces the structural-phase transition from cubic to mix cubic/hexagonal phase, which was proposed the planar defect such as stacking faults and twin along the (111) plane of c-GaN. These planar defects in the c-GaN film are generated from a rough surface of the AlGaAs buffer layer, which was observed for the films grown at high growth temperature. To decrease such planar defects in the c-GaN film, the growth condition

of AlGaAs buffer layer should be modified to obtain the flat surface of AlGaAs buffer layer. On the other hand, our results also suggest the lower growth temperature (900^{o}C) for c-GaN film to keep the surface of the AlGaAs buffer layer.

(ii) An anisotropic distribution of structural defects in the c-GaN film observed from TEM images taken from the [110] and [1$\bar{1}$0] zone is likely to be associated with the different atomic structure on (111) steps of surface along crystallographic direction on the (001) AlGaAs. Cross-sectional TEM images taken along the [1$\bar{1}$0] direction showed the less stacking faults and found treading dislocations at top area of c-GaN film. However, there is planar defect as twin along [$\bar{1}$1$\bar{4}$] zone axis which is observed by higher intensity of diffraction spot emerged with diffraction spot in the [1$\bar{1}$0] zone axis. DF-TEM images reveal the anti-phase domain boundary in c-GaN layer. The rough surface of AlGaAs buffer layer induces an anisotropic distribution of structural defects in c-GaN layer. Therefore, the less defect in c-GaN layer can obtain by improving the smooth surface of AlGaAs buffer layer.

(iii) Cubic-InN grown at relative high temperature can improve the flatness of surface and crystal quality of c-InN film. The hexagonal phase generation in c-InN film decreased with increasing growth temperature and In flux. The effect of hexagonal phase content in c-GaN buffer layer on hexagonal phase in c-InN film was observed by TEM. The hexagonal phase inclusion in c-InN films construct in a form of planar defect such as stacking faults and twins that are generated from an interface between c-GaN buffer layer and the c-InN film.

REFERENCES

[1] Porowski, S., and Grzegory, I., Thermodynamical properties of III–V nitrides and crystal growth of GaN at high N2 pressure, Journal of Crystal Growth 178 (June 1997) :174.

[2] Liliental, W.Z., Extended defects in bulk GaN and III-nitrides grown on this substrate, Journal of Crystal Growth 312 (September 2010): 2599.

[3] Hu, F.R.,Ochi, K., Zhao, Y.,Choi, B.S., and Hane, K., Molecular beam epitaxial growth of GaN thin film on Si substrate with InN as interlayer, Journal of Crystal Growth 294 (September 2006): 197.

[4] Zhu, X.L., and other, Structural characterization of InN films grown on different buffer layers by metalorganic chemical vapor deposition, Journal of Crystal Growth 306 (August 2007): 292.

[5] Briot, O., and others, Growth of InN films and nanostructures by MOVPE, Journal of Crystal Growth 31 (May 2009): 2761.

[6] Hsu, Y.J., Hong, L.S., Jiang, J.C. and Chang, J.C., Effects of hydrogen on GaN metalorganic vapor-phase epitaxy using tertiarybutylhydrazine as nitrogen source, Journal of Crystal Growth 266 (February 2004): 347.

[7] Hong, C.H., Pavlidis, D., Brown, S. W. and Rand, S. C., Photoluminescence investigation of GaN films grown by metalorganic chemical vapor deposition on (100) GaAs, Journal of Applied Physics 77 (February 1995): 1705.

[8] Grzegorczyk, A.P., Hageman, P.R., Weyher, J.L. and Larsen, P.K., Influence of sapphire annealing in trimethylgallium atmosphere on GaN epitaxy by MOCVD, Journal of Crystal Growth 283 (May 2005): 72.

[9] Kioseoglou, J., Polatoglou, H.M., Lymperakis, L., Nouet, G., and Komninou, P., A modified empirical potential for energetic calculations of planar defects in GaN, Computational materials science 27 (2003) 43.

[10] Available from http://park.itc.u-tokyo.ac.jp/onblab/research_e.html [2011,

May].

[11] Majewski, J. A., Hackenbuchner, S., Zandler, G. and Vogl, P., Nitride heterostructures: a system for high frequency electronics, Computational materials science 30 (2004): 81.

[12] Lin, J.C. and others, InN grown on GaN/sapphire templates at different temperatures by MOCVD, Optical Materials 30 (December 2007): 517.

[13] Ghazi, H. E., Jorio, A., Zorkani, I. and Ouazzani, M., Optical characterization of InGaN/AlGaN/GaN diode grown on silicon carbide, Optics Communications 281 (Februry 2008): 3314.

[14] Nakadaira. A., and Tanaka. H., Growth of Zinc-Blende GaN on GaAs (100) Substrates at High Temperature Using Low-Pressure MOVPE with a Low V/III Molar Ratio, Journal of Electronic Materials 26 (November 1997): 320.

[15] Wan, L., and others, Transmission electron microscopy study of hexagonal GaN film grown on GaAs (001) substrate by using AlAs nucleation layer, Journal of Crystal Growth 220 (August 2000): 379.

[16] Park, Y.J., Koh, E.K., Park, C.S., Park, I.W., and Kim, E.K., Thermal evolution of α- and β-Phases in the thin GaN on (001) GaAs, Thin Solid Films 41 (March 2002): 229.

[17] Kimura, R. and Takahashi, K. Investigation of the initial growth of cubic-GaN using an AlGaAs buffer layer grown on GaAs (1 0 0) by molecular beam epitaxy, Journal of Crystal Growth 227 (July 2001): 395.

[18] Kimura, R., Gotoh, Y., Matsuzawa, Y. and Takahashi, K., High-purity Cubic GaN grown on a AlGaAs buffer layer by molecular beam epitaxy, Journal of Crystal Growth 209 (February 2000): 382.

[19] Suandon , S., Sanorpim , S., Yoodee, K. and Onabe, K., Effect of growth temperature on polytype transition of GaN from zincblende to wurtzite, Thin Solid Films 515 (March 2007): 4393.

[20] Wu, J., Yaguchi, H., Onabe, K., Ito, R. and Shiraki, Y., Optical transitions in cubic GaN grown on GaAs(1 0 0) substrates by metalorganic vapor phase epitaxy, Journal of Crystal Growth 189-190 (June 1998): 415.

[21] Xie, Z.L., and others, The high mobility InN film Grown by MOCVD with GaN buffer layer, Journal of Crystal Growth 298 (January 2007): 409.

[22] Wang, J.B., Li, Z.F., Chen, P.P., Lu, W and Yao, T., Raman study of gap mode and lattice disorder effect in InN films prepared by plasma-assisted molecular beam epitaxy, Acta Materialia 55 (July 2007): 183.

[23] Zhu, X.L., and others, Structural characterization of InN films grown on different buffer layers by metalorganic chemical vapor deposition, Journal of Crystal Growth 306 (May 2007): 292.

[24] Ito, T., Akiyama, T., Nakamura, K., and Ito, T., Theoretical investigation On structural stability of InN thin film on 3C-SiC(001), Applied Surface Science 254 (February 2008): 7672.

[25] Jamil, M., Zhao, H., Higgins, J., and Tansu, N., Influence of growth temperature and V/III ratio on the optical characteristics of narrow band gap (0.77 eV) InN grown on GaN/sapphire using pulsed MOVPE, Journal of Crystal Growth 310 (November 2008): 4947.

[26] Chandrasekhar, D., Smith, .D.J, Strite, S., Lin, M.E., Morkoc, H., Characterization of Group III-Nitride semiconductors by high-resolution electron microscopy, Journal of Crystal Growth 152 (July 1995): 135.

[27] Wang, X., and Yoshikawa, A., Molecular beam epitaxy growth of GaN, AlN and InN, Progress in Crystal Growth and Characterization of Materials 48/49 (2004): 42.

[28] Liu, H. F., and others, MBE growth and Raman studies of cubic and hexagonal GaN films on (0 0 1)-oriented GaAs substrates, Journal of Crystal Growth 218 (September 2000): 191.

[29] Qu, B., and others, Orientation relationship between hexagonal inclusions and cubic GaN grown on GaAs(0 0 1) substrates, Journal of Crystal Growth 221 (2001): 399.

[30] Sanorpim, S., Katayama, R., Yoodee, K., and Onabe, K., Growth mechanism and structural characterization of hexagonal GaN films grown on cubic GaN (111)/GaAs (111)B substrates by MOVPE, Journal of Crystal Growth 275 (December 2005): 1023.

[31] Sanorpim, S., Takuma, E., Katayama, R., Ichinose, H., Onabe, K., and Shiraki, Y., Characterization of MOVPE-grown GaN layers on GaAs (111)B with a cubic-GaN (111) epitaxial intermediate layer, Physica Status Solidi b 240 (November 2003): 305.

[32] Fong, W.K., and others , Characterizations of GaN films grown with indium surfactant by RF-plasma assisted molecular beam epitaxy, Microelectronics Reliability 42 (2002):1179.

[33] Williams, D.B and Carter, C.B. Trasmission electron microscopy. Plenum Press, 1996.

[34] Thomas, G. Transmission electron microscopy of metals. Wiley, 1962.

[35] Shong, C.W., Haur, S.C. Science at the nanoscale : an introductory textbook. Pan Stanford Pub, 2010.

[36] Leng, Y. Materials characterization : introduction to microscopic and spectroscopic methods. John Wiley & Sons (Asia), 2008.

[37] Fultz, B. and Howe, J. M. Transmission electron microscopy and diffractometry of materials. 2nded, Springer, 2002.

[38] Edington, J.W. Practical electron microscopy in materials science. N.V Philips ,1976.

[39] Fernandez, J.R.L., and others., Near band- edge optical properties of cubic GaN, Solid State Communications 125 (January 2003): 205.

[40] Hu, G.Q., and others., Transmission electron microscopy and atomic force microscopy studies of GaN films grown on AlAs/GaAs(001) substrate, Journal of Crystal Growth 252 (May 2003): 517.

[41] Qin, Z.X., and others., High-resolution X-ray diffraction analysis of cubic GaN grown on (0 0 1)GaAs by RF-radical source molecular beam epitaxy, Journal of Crystal Growth 189-190 (June 1998): 42.

[42] Wu, J., Zhao, F., Onabe, K. and Shiraki, Y., Metalorganic vapor-phase epitaxy of cubic GaN on GaAs (1 0 0) substrates by inserting an intermediate protection layer, Journal of Crystal Growth 221 (December 2000): 276.

[43] Ishido, T., Funato, M., Hamaguchi, A., Fujita, A. and Fujita, S., AlAs/GaAs(0 0 1) as a template for c-oriented hexagonal GaN grown by metalorganic vapor-phase epitaxy, Journal of Crystal Growth 211

(December 2000): 280.

[44] Iwahashi, Y., Yaguchi, H. Nishimoto, A., Orihara, M. and Hijikata, Y., RF-MBE growth of cubic InN films on MgO (001) substrate, Physica status solidi(c) 6 (May 2006): 1515.

[45] Katayama, R. and Onabe, K., Fabrication of cubic and hexagonal GaN micro-crystals on GaAs (001) substrates with relatively thin low-temperature GaN buffer layer, Journal of Crystal Growth 278 (February 2005): 431.

[46] Bae, I., Seong, T., Park, P., and Kim, E., Structural Study of GaN Grown on (001) GaAs by Organometallic Vapor Phase Epitaxy, Journal of Electronic Materials 28 (1999): 873.

[47] Lee, H.J., Ryu, H., Lee, C. and Kim, K., Polytypes in GaN films grown by metalorganic chemical vapor deposition on (0001) sapphire substrate, Journal of Crystal Growth 191 (February 1998): 621.

[48] Walter, T. and Gerthsen, D., TEM analysis of epitaxial semiconductor layers with high stacking fault densities considering artifacts induced by the cross-section geometry, Ultramicroscopy 81 (October 2000): 279.

[49] Kuwano, N., and others., Trasmission Electron Microscopy Observation of Cubic GaN Grown by Metalorganic Vapor Phase Epitaxy with Dimethylhydrazine on (001) GaAs, Journal of Apply Physics 33 (January 1994): 18.

[50] Lebedev, V., Cimalla, V., Morales, F.M., Lozano, J.G., Gonzalez, D., Mauder, Ch. and Ambacher, O., Effect of island coalescence on structural and electrical properties of InN thin films, Journal of Crystal Growth 300 (February 2007): 50.

[51] Sanorpim, S., Takuma, E., Ichinose, H., Katayama, R. and Onabe, K., Structural transition control of laterally overgrown c-GaN and h-GaN on stripe-patterned GaAs (001) substrates by MOVPE, Physica Status Solidi b 244 (December 2006): 1769.

[52] Li, Yuan and Giling, L.J., Acloser study on the self-annihilation of antiphase boundaries in GaAs epilayer, Journal of Crystal Growth163 (November 1996): 203.

[53] Narayanan, V., Mahajan, S., Bachmann, K.J., Woods, V., and Dietz, N., Antiphase boundaries in GaP layers grown on (001) Si by chemical beam epitaxy, Acta Materialia 50 (October 2001): 1275.

[54] Kunert, B., Nemeth, I., Reinhard, S., Volz, K. and Stolz, W., Si (001) surface preparation for the antiphase domaim free heteroepitaxial growth of GaP on Si substrate, Thin Solid Film 517 (August 2008): 140.

[55] Nemeth, I., Kunert, B., Stolz, W., and Volz, K., Ways to quantitatively defect antiphase disorder in GaP films grown on Si(001) by transmission electron microscopy, Journal of Crystal Growth 310 (August 2008): 4763.

[56] Saman Kuntharin, " Structural analysis of cubic InN films grown by molecular beam epitaxy", (Degree of Master, Department of Physics, Faculty of Science, Chulalongkorn University, 2007)

[57] Ohba, R., Mitamura, K., Shimomoto, K., Fujii, T., Kawano, S., Ohta, J., Fujioka, H. and Oshima, M., Growth of cubic InN films with high phase purity by pulsed laser deposition, Journal of Crystal Growth 311 (March 2009): 3130.

VITAE

Miss Jamreonta Parinyataramas was born on Novemver 23, 1980 in Bangkok, Thailand. She has been a student in the Development and Promotion for Science and Technology talents project (DPST). She received her Bachelor degree of Science in Physics from Silapakorn University in 2002 and continued her Master's study in 2003.

She received her Master degree of Science in Physics from Chulalongkorn University in 2006 and continued her doctorial degree in 2006.

Conference Presentations and Publication:

[1] J. Parinyataramas, S. Sanorpim, C. Thanachayanont, K. Onabe, "Effect of AlGaAs buffer layer on defect distribution in cubic GaN Grown on GaAs (001) by MOVPE", The 16th International Conference on Crystal Growth (ICCG-16), Beijing, China, August 8-13, 2010.

[2] Jamreonta Parinyataramas, Sakuntam Sanorpim, Chanchana Thanachayanont, and Kentaro Onabe, "TEM Investigation of Anisotropic Defect Structure in Cubic GaN/ Al-GaAs/ GaAs (001) Grown by MOVPE", The International Workshop on Nitride semiconductors (IWN2010), the Marriott Tampa Waterside Hotel & Marina in Tampa, Florida, U.S.A., September 19 – 24, 2010.

[3] J. Parinyataramas, S. Sanorpim, C. Thanachayanont, K. Onabe, "TEM Investigation of Anisotropic Defect Structure in Cubic GaN/ AlGaAs/ GaAs (001) Grown by MOVPE", physica status solidi c 8 (October 2010): 2255.